NEW METHODS IN THE STUDY OF PROBLEMS IN STATISTICAL MECHANICS AND STOCHASTIC PROCESSES

Fabrizio Masullo

UNIVERSITAT ROVIRA i VIRGILI

New methods in the study of problems in Statistical Mechanics and Stochastic Processes

Fabrizio Masullo

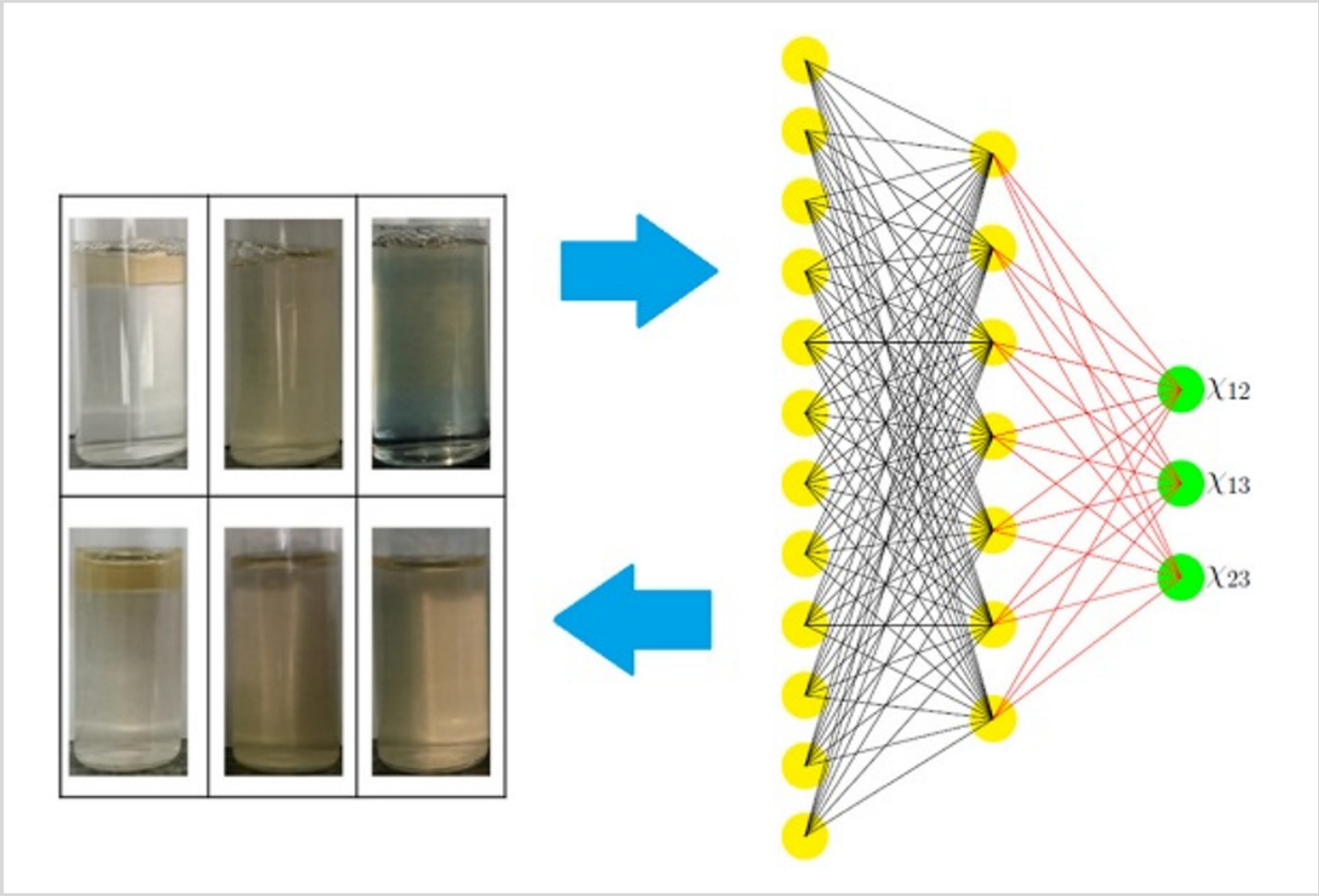

DOCTORAL THESIS
2023

New methods in the study of problems in Statistical Mechanics and Stochastic Processes

BY

Fabrizio Masullo

supervised by Profs.
Josep Bonet Avalos & Allan D. Mackie
Molecular Simulation Group
Departament d'Enginyeria Quimica

Universitat Rovira i Virgili
Tarragona, December 2023

UNIVERSITAT ROVIRA I VIRGILI
NEW METHODS IN THE STUDY OF PROBLEMS IN STATISTICAL MECHANICS AND STOCHASTIC PROCESSES
Fabrizio Masullo

Escola Tècnica Superior d'Enginyeria Química
Departament d'Enginyeria Química
Universitat Rovira i Virgili
Avinguda dels Països Catalans, 26
43007 Tarragona (Catalunya)

Tarragona, 8$^{\text{th}}$ of November 2023

We state that the present study entitled *New methods in the study of problems involving Statistical Mechanics and Stochastic Processes*, presented by Mr. Fabrizio Masullo for the award of de degree of Doctor, has been carried out under our supervision at the Departament d'Enginyeria Químcia, of the Universitat Rovira i Virgili de Tarragona.

PhD. supervisor

Prof. Josep Bonet Avalos

PhD. co-supervisor

Prof. Allan D. Mackie

UNIVERSITAT ROVIRA I VIRGILI
NEW METHODS IN THE STUDY OF PROBLEMS IN STATISTICAL MECHANICS AND STOCHASTIC PROCESSES
Fabrizio Masullo

To my wife Veronica.

UNIVERSITAT ROVIRA I VIRGILI
NEW METHODS IN THE STUDY OF PROBLEMS IN STATISTICAL MECHANICS AND STOCHASTIC PROCESSES
Fabrizio Masullo

Abstract

This work is focused on the development of advanced computational tools for prediction and control of scientific phenomena.

Firstly we apply Artificial intelligence to Computational Chemistry. In particular, in this first part, we deal with water-in-water (W/W) emulsions which is a new drug delivery system. Our research is devoted to the ternary system composed of water, gelatine and maltodextrin, which is a fundamental W/W emulsion of great importance in food production. Aiming at controlling the phase diagram of such a ternary system we develop a numerical approach, based on the Flory-Huggins (FH) theory, with an application of a Neural Network (NN) non-linear regression. In our computational method, the NN is trained with a big number of different numerical experiments. To be more specific, we have a fixed set of different initial compositions and in each simulated experiment, we change the FH-parameters, and we numerically produce the final number of phases expected by the FH model. Consequently we get the FH-predicted phase diagrams of the initial compositions ensemble, depending on the chosen FH-parameters. Once the NN is trained with all these FH-simulated phase diagrams, we can infer the FH-paramters that best describe our ternary system by applying the trained NN to the real phase diagram experimentally obtained for the same set of initial concentrations. Our predictive approach seems to be very effective because it provides also the final concentration of the phases at equilibrium which are in perfect agreement with the final experimental concentrations obtained with the Raman spectroscpy. The interesting feature of this method is that the concentration of the phases at equilibrium are not *a priori* known and the only required information to train the NN are the number of phases at equilibrium of each initial concentration.

Secondly we focus on Random differential Equations (RDE) which are a specific class of Stocastic Differential equations (SDE) in which randomness affects only the initial data. These features make RDEs a central tool in prediction and control of scientific phenomena and for the study of the time evolution of a physical system. In particular we consider the case of RDE that are originated as an Ordinary Differential Equations (ODE) Cauchy-initial values problem with only one random

initial data. These type of RDE turn to be equivalent to the very well known and very old (RVT) problem of the transformation of a Random Variable (RV) X into a new RV $Y = g(X)$ under the action of a given function g. This very well known problem of Probability Theory is perfectly solved when the transformation function g is invertible. However such a RVT problem becomes very complex if g is not invertible, although is theoretically possible. Our contribution provides a new mathematical description of functions that allows to easily find all the pre-images of a given function g in the case of non-invertibility of g. Then, with our work, the RVT problem can be easily solved. Consequently our theoretical contribution can be implemented to produce a very effective and precise algorithm to solve the above mentioned RDE with a very low computational cost. Due to the generality that characterise the RVT problem, the proposed research may have *a plethora* of applications in Mathematics, Statistics and Computational Physics.

Acknowledgements

First of all, I want to acknowledge my thesis Advisor Professor Josep Bonet Avalos, who gave me the opportunity to learn from his extraordinary scientific knowledge. Without his support, guidance and kindness, this work would have not been possible. I must also acknowledge him to have been like a father for me in the hard times of the PhD. An extraordinary acknowledge goes to Professor Fabio Zanolin, another Great Master of my life which helped me so many times along my very short scientific carrier. I am also grateful to all the members of the Molecular Simulation Group of the University Rovira i Virgili of Tarragona. A particular acknowledge goes to professor Allan Donald Mackie for the great humanity of is support. A great acknowledge goes to my colleges Berardo Mario Manzi and Maria Pantelidou. Along these years, I also received a fundamental support from two amazing women which are Teresa Marmol and Nuria Juanpere, to whom I extend my deepest thanks. Finally I must acknowledge an extraordinary professor that supports me in many ways which is professor Gustavo Orozco of the Universidad Nacional de Colombia.

Since this thesis is the last event of more than twenty years of studies, I desire to thank all the teachers of primary and secondary school and all the university professors that helped me in reaching this day. Among all I want to acknowledge my teachers of the secondary school Patrizia Fiermonte, Giuseppina Trifiletti and my mentor Roberto Grison and his wife Annamaria Pertoldi. Furthermore I thank my extraordinary university Masters of the University of Udine: Dikran Dikranjan, Paolo Cragnolini, Paolo Giannozzi, Maurizio Trombetta, Paolo Baiti and Dario Fasino.

At last but not least, I must acknowledge all the members of my family. First of all my amazing wife Veronica for supporting me and for being so patient with me and with my madness. Secondly I acknowledge my little boy Leonardo for his love. Furthermore this thesis would not be possible without the huge love and education received from parents Francesca and Luigi and my brother Riccardo, their support has been too important along almost my life. I thank a lot also my parents in law Francesca and Sandro and my very brilliant sister in law Irene

for their fundamental support. Since this thesis is the end of a huge path I must acknowledge all the friends and the relatives that supported me along my life. The list is huge and I cannot mention all of them. However, I must mention Paola Sguazzero, a very kind relative whose support has been very important. I thank all my friends for their great support along my life, in particular: Dario Pupillo, Alfredo Blessano, Gianmaria Niccodemi. I must also mention some new great friends of mine which are another extraordinary gain of my permanence in Tarragona. In particular I acknowledge Antonio Cruz and his wife Cristina and their amazing daughter Elanor, for have been my family in Tarragona. I want to thank a really promising student Marc Arenas Cruz which is my best friend in Reus. Finally I acknowledge a great friend of mine, Pezhman Kazemi.

Contents

List of Figures

List of Tables

Chapter 1

Introduction

In science a challenging approach is to look for connections between different research areas. Indeed, some of the most important scientific results arise precisely because an unexpected connection between different subjects of knowledge has been noticed (see for example Ref. [19]). Over the last few decades, this approach has been the core tool in some highly effective research fields, like computational physics and computational chemistry. In the last fifty years, these two subjects have received a huge amount of interest due to the extreme importance of numerically predicting the outcome of a physical or chemical experiment, and the use of numerical modelling for the design of new products and new processes (see for example Refs. [19], [20]). Indeed, the possibility of mimicking an experiment or an engineering product manufacturing process with a computer simulation drastically reduces investments in time, resources, and consequently saves money.

As a further example of a great challenging research field, which has been impressively developed in recent years, we mention the ensemble of statistical methods introduced in order to reconstruct phenomena from data analysis. These approaches have been developed only after the diffusion of computers because they are effectively applicable only through a huge computational power. We stress that such approach to scientific problems constitutes a revolutionary innovation. Indeed, the common research of the last centuries has focused on finding the laws that govern nature, and then, the validity of theoretical results has been verified by experiments. In the statistical methods mentioned earlier, a significant amount of data is collected from experiments and the theoretical model is deduced from the analysis of the data. Among these methods the one which is receiving the biggest interest is *Artificial Intelligence (AI)*. In the literature we can find a *plethora* of research papers developed in the last decades that deals with AI. As noticed in Ref. [21], a deep understanding of how the mind perceives, thinks, and acts and its imitation will have a revolutionary impact in science, medicine, economics and many

other subjects of research. For example as reported in Ref. [22], AI approaches are increasingly being considered across different chemical disciplines. Furthermore in Ref. [22] is mentioned how AI is expected to make a huge revolution also in drug discovery and development. In Ref. [23] is reported that conditions exist for AI to play a crucial role also in chemical engineering. And finally in Ref. [24] is said that AI is expected to have a revolutionary impact across nearly the entire domain of materials and structures, processes, multi-scale modelling and simulation over the next two decades.

Trying to summarize the present work, we may refer to the above mentioned intent to connect different subjects of science. In particular this thesis has been developed trying to apply pure theoretical mathematical models to applied problems. To be more specific the problems of interest concern Computational Chemistry and Computational Physics.

In the first research project we developed a procedure to determine some chemical parameters (the Flory Huggins parameters), that characterize a mixture of polymers, by applying Artificial Intelligence. The information required consisted of only the experimental phase diagram of the mixture. This project was fascinating because it demanded knowledge of diverse research subjects and involved individuals with diverse backgrounds. Furthermore this work has a double application. The first one is most apparent because the results offer FH parameters that represent a particular polymer mixture, and these parameters can be immediately used to predict the outcome of concrete experiments. The second, more theoretical application, is the strategy of introducing an AI approach to chemistry. This approach can be repeated with diverse mixtures and possibly with other theoretical models that differ from Flory-Huggings.

In the second research project we developed a novel theoretical framework that allows us to solve the Random Variable Problem (RVT) in the presence of a non-invertible function. In view of the generality of the theoretical problem that we solved, this result has many applications in different fields of research like Probability, Statistics, Computational Physics, among others. Although this result has such a big amount of possible applications, in this thesis we concentrate in particular to its interest for Computational Physics. To be more specific we addressed the problem of solving Random Differential Equations in which we have a dynamical system that evolves following deterministic laws, but has some randomness affecting one initial parameter, i.e. the initial conditions.

Summarising, this thesis is divided into two distinct parts:

1. The first part deals with Computational Chemistry and its approach is

based on data reconstruction method (in particular Neural Networks) used to parametrise a Flory-Huggins model for a particular polymer mixture.

2. The second part deals with Computational Physics. In particular, we address the problem of constructing an efficient algorithm for the generation of the time-dependent probability distribution generated by the randomness of the initial conditions in a general dynamic process, with application to multiple fields in experimental sciences.

In what follows we provide a more detailed description of the subjects addressed in this thesis.

Part 1: Application of AI to the parametrisation of a Flory-Huggins model from experimental data

Water in oil or *oil in water* emulsions have been for long time used for nano and micro-particles delivery system for food and biomedical applications. To better preserve biocompatibility of drug delivery systems (DDS)Ref. [1], an interesting alternative is *water-in-water (W/W) emulsions* as templates to obtain such DDS. Water-in-water emulsions are colloidal dispersions made of two or more water-soluble polymers which are mutually immiscible under some thermodynamic conditions of interest. Such mixtures of two hydrophilic polymers in aqueous solution can produce three different phase behaviours Ref. [2]:

1. A complete miscibility, in the case of weak repulsive/attractive interactions between the two polymers,

2. Associative phase separation (coalescence) with formation of a precipitate/coacervate, if the attractive interactions between the two polymers are strong,

3. Segregative phase separation induced by repulsive interactions between the polymers.

The third situation is the one that leads to two-phase systems in which W/W emulsion droplets can be formed by dispersing one minority phase into the bulk of the other Ref. [2]. Therefore, the control of the phase diagram of aqueous mixtures phases is a key tool to create such W/W emulsions, with a dispersion of soft nanoparticles, which can be further crosslinked aiming at biomedical applications. Among all the ternary systems, the one composed of water, gelatin and maltodextrin has been the focus of great attention Refs. [3, 4, 5, 6, 7] because of the biocompatibility of both polymers. Indeed, aqueous two-phase systems (ATPS)

based on gelatin are used for the formation of gelatin microgels Ref. [6], which are edible and thus can be used in food applications.

In this thesis we create a numerical framework, based the Flory-Huggins (FH) theory, able to reproduce experimental results. In particular, we find numerical values for the Flory-Huggins χ-parameters (FH parameters) of the system water-gelatin-maltodextrin, through a non-linear regression of numerical results, used as the training set of a Neural Network (NN), then using the phase diagram obtained with experiments to obtain the parameters of the corresponding predictive model. The experimental data provided concerned only the final number of phases obtained in function of the initial compositions, but no further information was provided about the concentrations of the phases in equilibrium. Due to the lack of such a detailed information on the concentrations of the coexisting phases, the process of fitting FH parameters becomes extremely complicated as it relies only on the dependence of the phase boundaries on the model parameters. By using numerically generated phase boundaries from simulation, we could provide this information to a neural network and fit the model parameters for the experimental results. The benefit of having an adjusted FH model is that we can thus predict the composition of the phases in coexistence and explore regions of interest even before the experimentation is done.

Part 2: Random Variable Transformation Technique for Computational Physics

The development of Modern Physics has often required some probability models to describe systems and processes that are stochastic, because of the ignored or non-accessible variables, or intrinsically probabilistic, as in Quantum Mechanics. Thus, due to the impossibility of controlling all the parameters of a physical experiment or an engineering process, stochastic models relying on one or more probabilistic parameters have been introduced (See Refs. [17], [18]). From the formal point of view, most of the problems are treated with Stochastic Differential Equations (SDE) and/or Random Differential Equations (RDE) like the celebrated Langevin equation (See Ref. [16]). An SDE is a differential equation in which the time-evolution of one or more parameters is not well determined and is represented by a Random Variable (RV), whose properties are known *a priori*. An RDE is a special type of SDE in which the randomness affects only initial data. The mathematics that underline an SDE is extremely complex. However, in the case of RDE, the problem can be treated as a Random Variable Transformation technique RVT. Indeed, the randomness affects only initial data, while the evolution of the system is completely deterministic through a dynamic mapping between the initial probability distribution and the final one after the system is allowed to evolve

according to a given dynamics. Hence, the RVT acts as a function that transforms the probability distribution function of the initial data. This model is of great interest in Computational Physics. To stress the huge interest of RDE problem we mention some classical RDE problems of Theoretical and Computational Physics that we consider in this thesis. In particular we deal with the *Logisitc map*, which is known to yield chaotic dynamics, with random initial point. Furthermore we consider also the pendulum equation in the particular case in which the initial phase is affected by randomness, and some other examples of interest.

In this part we explore the complex field of Random Variable Transformation methods aiming at solving RDE problems for applications in Physics, Chemistry, Biology or Engineering. For this kind of problem, a huge number of important results can be found in the literature (see for example Refs. [10, 11, 12, 13, 14, 15]). However, most of these methods apply to the particular case in which the deterministic transformation of variables is invertible, i.e. the mapping is invertible. Hence, most of them can not be applied to specific problems because in most relevant cases, the mapping g_t is far from being bijective and then also far from being invertible. The algorithm we have developed is called Folding Domain Function (FDF) and it is applicable to non invertible RVT problems. We warn the reader that, for the moment, our method is applicable only to the particular case in which the RVs are scalar random variables, and the mapping function is a one-variable real function. Our hope is that this method will be extended to higher dimensions in the future. Furthermore, we stress that in most of the physical problems the mapping function g_t is obtained as the solution of a differential equation which cannot be determined analytically but only numerically. Then, the interest of our contribution is evident because our method is applicable to systems where g_t can only be obtained numerically.

In conclusion, the work presented in this thesis is a successful attempt at applications of new techniques to the modelling of relevant problems of experimental sciences. Far from being a simple theoretical exercise, we think that the objectives achieved are of relevant practical importance in real world applications. We expect that the scientific society will honour the new developments presented in this thesis by applying them to future problems.

Bibliography

[1] Beldengrün, Y.; Aragon, J.; Prazeres, S.; Montalvo, G.; Miras, J.; Esquena, J. **Gelatin-Maltodextrin Water-in-Water (W/W) Emulsions for the Preparation of Crosslinked Enzyme-Loaded Microgels.** *Langmuir.* **2018**, *34*, 9731-9743.

[2] Singh, P.; Medronho B.; Miguel M.G.; Esquena, J. **On the encapsulation and viability of probiotic bacteria in edible carboxymethyl cellulos-gelatin water-in-water emulsions.** *Food Hydrocolloids.* **2017**, *75*, 41-51.

[3] Lorén, N.; Hermansson A. **Phase separation and gel formation in kinetically trapped gelatin/maltodextrin gels.** *Int J Biol.* **2000**, *27*, 249-262.

[4] Nawong, S.; Oonsivilai, R.; Boonkerd, N.; Truelstrup Hansen, L. **Entrapment in food-grade transglutaminase cross-linked gelatin-maltodextrin microspheres protects Lactobacillus spp. during exposure to simulated gastro-intestinal juices.** *Food Res Int.* **2016**, *85*, 191-199.

[5] Kasapis, S.; Morris, E.R.; Norton, I.T.; Clark, A.H. **Phase equilibria and gelation in gelatin/maltodextrin systems — Part IV: composition-dependence of mixed-gel moduli.** *Carbohydr Polym.* **1993**, *21(4)*, 269-276.

[6] Alevisopoulos, S.; Kasapis, S.; Abeysekera, R. **Formation of kinetically trapped gels in the maltodextrin—gelatin system.** *Carbohydr Res.* **1996**, *293(1)*, 79-99.

[7] Kasapis, S.; Morris, E.R.; Norton, I.T.; Clark, A.H. **Phase equilibria and gelation in gelatin/maltodextrin systems — Part I: gelation of individual components.** *Carbohydr Polym.* **1993**, *21(4)*, 243-248.

[8] Huang, K.; **Statistical mechanics 2nd edition.** *John Wiley & Sons* **1987**.

[9] Tuckerman, M. E.; **Statistical Mechanics: Theory and molecular simulations. 1st edition** *Oxford university press* **2010**.

[10] Cortés, J.-C. and El-Labany, S. K. and Navarro-Quiles, A. and Selim, M. M. and Slama, H. **A comprehensive probabilistic analysis of approximate SIR-type epidemiological models via full randomized discrete-time Markov chain formulation with applications**. *Mathematical Methods in the Applied Sciences* **2020**, *43,14*, 8204–8222.

[11] Cortés, J.-C. and López-Navarro, E. and Romero, J.-V. and Roselló, M.-D. **Probabilistic analysis of a cantilever beam subjected to random loads via probability density functions**. *Computational & Applied Mathematics* **2023**, *42,1*, 32.

[12] Murray, J. D. **Mathematical biology. I**. *Interdisciplinary Applied Mathematics, Springer-Verlag, New York* **2002**.

[13] Calatayud, J. and Cortés, J. C. and Dorini, F. A. and Jornet, M. **Dealing with variability in ecological modelling: an analysis of a random non-autonomous logistic population model**. *Mathematical Methods in the Applied Sciences* **2022**, *45,6*, 3318–3333.

[14] Casabán, M.-C. and Cortés, J.-C. and Navarro-Quiles, A. and Romero, J.-V. and Roselló, M.-D. and Villanueva, R.-J. **A comprehensive probabilistic solution of random SIS-type epidemiological models using the random variable transformation technique**. *Communications in Nonlinear Science and Numerical Simulation* **2016**, *32*, 199–210.

[15] Casabán, M.-C. and Cortés, J.-C. and Navarro-Quiles, A. andì Romero, J.-V. and Roselló, M.-D. and Villanueva, R.-J. **Probabilistic solution of the homogeneous Riccati differential equation: a case-study by using linearization and transformation techniques**. *Journal of Computational and Applied Mathematics* **2016**, *291*, 20–35.

[16] P. Langevin **Sur la théorie du mouvement brownien**. *C. R. Acad. Sci. (Paris)* **1908**, *146*, 530-533.

[17] N.G. Van Kampen **Stochastic Processes in Physics and Chemistry (Third Edition)**. *Elsevier,North-Holland Personal Library* **2007**, 193-218.

[18] Crispin Grandiner **Stochastic Methods: A Handbook for the Natural and Social Sciences**. *Springer, springer series in synergetics* **2009**.

[19] Z. Shen, L. Yang, J. Pei, M. Li, C Wu, and J. Bao, T. Wei, Z. Di, R. Rousseau and J. Wu. **Interrelations among scientific fields and their relative influences revealed by an input–output analysis**. *Elsevier, Journal of Informetrics*. **2016** *1(10)*, 82-97.

[20] Richard Khoury, Douglas Wilhelm Harder **Numerical Methods and Modelling for Engineering**. *Springer Cham*, **2018**.

[21] Pier Luigi Gentili **Small steps towards the development of chemical artificial intelligent systems**. *RSC Adv.*, **2013** *3*, 25523.

[22] F. Miljković, R. Rodríguez-Pérez, and J. Bajorath **Impact of Artificial Intelligence on Compound Discovery, Design, and Synthesis**. *ACS Omega*, **2021** *6*, 33293-33299.

[23] Venkat Venkatasubramanian **The Promise of Artificial Intelligence in Chemical Engineering: Is It Here, Finally?**. *Wiley Online Library*, **2019** *65(2)*, 466-478.

[24] D. M. Dimiduk, E. A. Holm and S. R. Niezgoda **Perspectives on the Impact of Machine Learning, Deep Learning, and Artificial Intelligence on Materials, Processes, and Structures Engineering**. *Integrating Materials and Manufacturing Innovation*, **2018** *7*, 157-172.

Chapter 2

Phase behavior of gelatin/maltodextrin aqueous mixtures studied from a combined experimental and theoretical approach

2.1 Introduction

Aqueous two-phase systems, often abbreviated as ATPS, are commonly found in mixtures of slightly incompatible hydrophilic components that form two immiscible phases, with water as the common solvent [1, 2, 3, 4]. Water-water phase separation into two phases is a common phenomenon, which can be found in a wide variety of aqueous mixtures. These include combinations of polymers and electrolytes, polymers and surfactants, mixtures of polymers and mixtures of surfactants, among others. Moreover, in some cases, separation into two aqueous phases can also be found in solutions of a single component in water. For example, aqueous solutions of nonionic surfactants, at temperatures above the so-called cloud point, separate into a surfactant-rich solution and a surfactant-depleted solution, where both phases contain water as common solvent.

Water/water phase separation, in the presence of certain solutes or a combination of two solutes, has been known for a long time[1, 5, 6]. The microbiologist Beijering [1], while culturing cells in 1896 observed that droplets were formed in his culture media when mixing gelatin and hydrolysed starch solutions. He also noticed that both starch-in-gelatin and gelatin-in-starch emulsion droplets could be pro-

duced depending on the specific starch/gelatin mass ratio. In addition, Beijering described that a similar behavior occurs in agar and gelatin aqueous mixtures [6]. Although these early works were very accurate in describing such curious phase behavior, they did not result in commercial applications. More recently, ATPS have been used for different purposes, including the extraction of biomolecules in complex biological fluids, for which many examples can be found in the literature [3]. This capacity of the ATPS for extraction and purification processes has made them a subject of particular interest.

Since both phases in ATPS mainly consist of water they constitute a very mild environment for the extraction of biomolecules due to the absence of organic solvents and aggressive conditions. Furthermore, the low interfacial tension between the two aqueous phases makes mass transfer across the interface to be almost unaffected by its presence, thus favoring extraction. For example, in early reports of extraction processes in ATPS, Albertsson and co-workers described that ATPS in water/dextran/methylcellulose mixtures were very effective for the fractionation and concentration of viruses [7, 8]. They reported that several viruses become significantly concentrated in the dextran phase, thus allowing their extraction through liquid/liquid fractionation without affecting the virus viability [7]. The same principle can be used for the extraction of proteins in complex mixtures of biological fluids [9]. After these pioneering works, ATPS became a very powerful and versatile tool for separation and extraction of many different biomaterials [10].

Aqueous liquid/liquid phase separation is a rather general phenomenon in aqueous mixtures of mutually non-attractive polymers. Many hydrophilic polymers show incompatibility in aqueous solutions, resulting in phase separation into two coexisting aqueous phases, each phase enriched with one of the polymers, and sometimes even three phases. For example, around 100 different aqueous mixtures of proteins and polysaccharides that result in phase separation have been mentioned in a review paper [11]. In particular, the ternary system composed of water, gelatin and maltodextrin has been the focus of great attention [12, 13, 14, 15, 16]. Aqueous mixtures of biopolymers in the presence of gelatin are highly interesting because of the jellifying properties of gelatin, which forms elastic hydrogels at temperatures below $\simeq 35°C$, depending on the nature of gelatin, its molecular weight and charge density. ATPS based on gelatin have been thus extensively studied, as these systems are used for the formation of gelatin microgels [15], which are edible and thus can be used in food applications. In a previous work, gelatin microgels have shown to be useful for the encapsulation of enzymes, and the velocity of release can be controlled by the degree of gelatin cross-linking [17]. Therefore, the H_2O/gelatin/maltodextrin system might have a great potential in therapeutic applications. The phase behavior of this system is complex and is not completely understood. First, gelatin often undergoes a conformational transition from ran-

dom coils to elongated rigid self-assemblies, forming elastic hydrogels, typically at temperatures below 35°C [18]. Second, gelatin/maltodextrin aqueous mixtures show an unusual precipitation at low concentrations below the binodal line of liquid/liquid phase separation. A solid-like precipitate (S phase) appears, being attributed to changes in conformation in maltodextrin induced by the presence of gelatin[19]. The study of the phase behavior of such complex mixture, prone to conformational changes of its components, which are of natural origin and therefore of varying characteristics, is very challenging.

In this article we study in detail the phase behavior of gelatin-maltodextrin aqueous solutions aiming at their use for the formation of nanogels for drug delivery. In particular, we propose a mathematical model able to reasonably predict the phase diagram and compositions of the phases, which is of use for nanogel formulation. The results of the present analysis should permit in the future the determination of the appropriate parameters for the manufacturing of tailor-made nanogels based on the phase behavior of these polymers.

In view of the ultimate purpose of the controlled manufacturing of nanogels, we have accompanied the experimental study with a theoretical analysis based on the Flory-Huggins theory. We have determined an appropriate Flory-Huggins description that reasonably reproduces the experimentally found phase diagrams at low concentrations. It is relevant to mention that, due to the lack of detailed information of the concentrations of the phases in equilibrium, the process of fitting Flory-Huggins parameters (FH parameters, from now on) from experimental data is performed using non-linear regression based on neural networks. With this goal, we have calculated the phase diagram for a large set of different FH parameters, obtaining the number of phases over the same points (states) for which experimental data has been gathered. A neural network (NN) is then trained from the numerical data generated in this way. The trained NN thus contains the information that links the values of the FH parameters to the form of the phase diagram. The best fit of the FH parameters for gelatin-maltodextrin aqueous mixtures is then obtained from the prediction of the NN based on a regression of the experimental data. Although this is a novel method conceived to extract the maximum information from the available data, we want to point out that such relevant information for the NN regression is limited to the phase boundary region and, therefore, it is very important to adequately fit the phase boundary between one phase (L) and two phases ($L + S$), as will be discussed later on.

Despite the known limitations of the Flory-Huggins theory, the analysis presented here provides a rather quantitative description of this system for one temperature and two pH values that are relevant for the preparation of emulsions and microgels [17]. The model is able to provide an estimate of the thermodynamic behavior of the mixture and therefore can be used to predict the appropriate con-

ditions for subsequent experimental studies. Certainly, the present work allows for the understanding of the behavior of gelatin/maltodextrin mixtures, the complexity of which has not yet been completely unraveled.

2.2 Theoretical analysis of the phase behavior of aqueous polymer mixtures

The phase behavior of segregative systems was studied in detail by Lindman and Piculell [20], among others. They described the phase behavior of many systems that display phase separation in mixtures of two hydrophilic components (two polymers or mixtures of a polymer and a surfactant). These authors also showed that this segregative phase behavior occurs frequently provided that the two components do not have attractive interactions [21]. Lindman and Piculell focused their attention on the phase behavior (either aggregation or segregation) of surfactant-polymer aqueous mixtures [22, 23]. In aqueous mixtures of two hydrophilic polymers the typical phase behavior can be described using the Flory-Huggins theory [24, 25, 26].

The thermodynamics of polymers in solutions differ from ordinary binary mixtures [23, 24, 27] in that the connectivity of polymer molecules strongly reduces the entropy of mixing, as compared with the one of free monomers. Flory and Huggins [25, 26] independently proposed a model for the calculation of the Gibbs free energy of mixing from statistical mechanical principles [28, 29, 30]. This theory is based on a microscopic representation of the system in a lattice fully occupied by either monomers or solvent molecules. Thus, for a ternary system with two polymers in solution, the solvent molecules occupy n_1 sites, while the monomers occupy n_2 and n_3 lattice sites, respectively. These occupation numbers satisfy $n_1 + n_2 + n_3 = N$, where N is the total number of lattice sites, equivalent to the total volume of an incompressible system. In the Flory-Huggins theory, all species are considered to have the same molecular volume v. The volume fraction of the i^{th} species is denoted by ϕ_i.

Flory and Huggins demonstrated that the entropy of mixing, ΔS_M, for a ternary system involving two polymers and a low molecular weight solvent is given by (2.1),

$$\Delta S_M = -NR\Big(\phi_1 \ln \phi_1 + \frac{\phi_2}{r_2} \ln \phi_2 + \frac{\phi_3}{r_3} \ln \phi_3\Big) \tag{2.1}$$

where r_2 and r_3 are, respectively, the polymerization indices of each polymer. Notice that the entropy of mixing is always positive. Therefore, it always favors the mixing of the components. To complete the description, the enthalpy of mixing

is also required. FH proposed a simple model based on the average number of contacts between the different species. The final expression takes the form

$$\Delta H_M = NRT \sum_{i,j>i}^{3} \chi_{ij}\, \phi_i \phi_j \tag{2.2}$$

where χ_{ij} are the so-called Flory-Huggins parameters, which define the excess enthalpic interaction between species (see ref. [31] for a detailed discussion). A negative Flory Huggins parameter $\chi_{ij} < 0$ thus indicates that the interaction between unlike species is preferred to the self interactions, thus favoring the mixing. Conversely, a high positive Flory Huggins parameter indicates that the self interactions are preferred and hence the enthalpy contribution favors the demixing of the solution.

Finally, using the fact that at constant T

$$\Delta G_M = \Delta H_M - T\Delta S_M \tag{2.3}$$

one arrives at the Gibbs free energy of mixing of the solution, namely,

$$\Delta G_M = NRT \left[\phi_1 \ln \phi_1 + \frac{\phi_2}{r_2} \ln \phi_2 + \frac{\phi_3}{r_3} \ln \phi_3 + \sum_{i,j>i}^{3} \chi_{ij}\, \phi_i \phi_j \right]. \tag{2.4}$$

Phase equilibria based on this approach has been demonstrated to be essentially correct, as shown for example by A.H. Clark [32], who was able to fit experimental tie-lines in ternary mixtures to such theoretical models. The FH model is in general better suited for relatively concentrated solutions of non-polar molecules due to its intrinsic characteristics, such as zero volume of mixing or the neglect of intrachain correlations in the enthalpy calculations, among others. Moreover, the FH approach is quite successful in describing the behavior of ternary systems composed of water-soluble molecules in water, although one must pay the price of defining FH parameters that depend on thermodynamic variables such as temperature, concentrations, or on the ionic strength of the solution, for example.

As far as the phase diagrams are concerned, the entropy of mixing in systems of two long polymers and a low molecular weight solvent is dominated by the solvent contribution. This explains the strong asymmetry of the diagrams. Therefore, in ternary systems with two long polymers, these aforementioned small contributions due to the polymers' entropy of mixing make their phase diagram depend mainly on the values of enthalpic FH parameters [33, 34, 35]. For a general reference see for instance [31].

Since the system described by (2.4) is incompressible, one has that

$$V = v_1 n_1 + v_2 n_2 + v_3 n_3 \tag{2.5}$$

Hence, the number of solvent molecules n_1 can be actually replaced by a combination involving the solution volume and the number of moles of monomers of the two polymers. Within this context, one can define the osmotic pressure as

$$\Pi = -\left(\frac{\partial \Delta G_M}{\partial V}\right)_{T,n_2,n_3} \tag{2.6}$$

and the so-called exchange chemical potentials $\overline{\mu}_i$, with $i = 2, 3$ as

$$\overline{\mu}_i = \left(\frac{\partial \Delta G_M}{\partial n_i}\right)_{T,V,n_j} \tag{2.7}$$

While the osmotic pressure is the excess pressure due to the presence of the solute, the exchange chemical potential stands for the change in free energy per molecule when exchanging a given volume of monomer by the equivalent volume of solvent. Therefore, two phases, namely α and β, are in equilibrium if

$$\begin{aligned} \Pi^\alpha &= \Pi^\beta \\ \overline{\mu}_2^\alpha &= \overline{\mu}_2^\beta \\ \overline{\mu}_3^\alpha &= \overline{\mu}_3^\beta \end{aligned} \tag{2.8}$$

These are three non-linear algebraic equations whose solution provides the composition of each phase given the composition of the initial homogeneous state.

2.2.1 Numerical solution of phase equilibria

In view of the computational power available, we have developed a method inspired by the so-called Monte Carlo Gibbs ensemble [36]. A system with an overall volume fraction of water $\overline{\phi}_1$ and compositions of gelatin $\overline{\phi}_2$ and maltodextrin $\overline{\phi}_3$ (the overline stands for the compositions of the starting homogeneous system) with a volume V, is split into three boxes. Each box is assigned an initial volume and composition that satisfy the overall constraints of total volume and moles of each species. Such an initial state is conveniently varied to initialise the free energy minimization in different runs. For each MC step in a given run a pair of boxes is chosen at random and an exchange is proposed between these boxes of either gelatin, maltodextrin or simply volume. The overall new free energy $\mathcal{F}_{new}$ after the exchange is compared with the old one $\mathcal{F}_{old}$. The exchange is accepted if the former is lower than the latter and rejected otherwise. Since we are only seeking to minimise the free energy, the issue about fluctuations and the application of the appropriate Metropolis criterion, for example, are disregarded in favor of the aforementioned acceptance rule. However, there are a couple of aspects that

should be taken into account. First of all, the proposed exchanges are such that the total volume of the system V as well as the total number of moles of both gelatin $n_2 = \overline{\phi}_2 V/v_2$ and maltodextrin $n_3 = \overline{\phi}_3 V/v_3$ are kept constant. Second, the possibility of extremely low concentrations in the dilute phase is maintained by forcing an equal probability rule of 0.5 of either increasing or decreasing any concentration. We apply this rule according to the following. When a volume fraction is either negative or bigger then 1, the size of the concentration exchange initially proposed is reduced until the final concentration lies within the physical bounds. Afterwards, the acceptance check is invoked. The violation of detailed balance that this procedure implies is immaterial for our purpose of finding the minimum energy, since no sampling of the fluctuations in the Gibbs ensemble is required.

We have performed these Monte Carlo runs for up to 10^7 steps, starting from different initial states for the same system, to avoid getting trapped in metastable states. At the end of the process, one finds three possible scenarios: either i) the same composition is found in the three boxes, indicating that the phase equilibrium is consistent with one single phase, or ii) one box has a composition different from the other two, indicating that there are two phases in equilibrium, or iii) the three boxes have different compositions, in which case there are three phases. The true equilibrium of the final outcome is guaranteed by checking that eqs. (2.8) are satisfied by each pair of boxes. The numerical approach described so far, involving the calculation with three boxes that reach mutual thermodynamic equilibrium, allows the system to reveal three phases where they exist. Therefore, we are sure that the one and two-phase regions found are indeed such.

The procedure yields the equilibrium phases after some 10^5 MC steps, for points that lie far from the phase boundary. This number is sometimes increased for the states near the phase boundary, where the free energy difference between the scenarios is rather small. In these cases, the final free energies obtained in different runs are compared and we choose the lower one as the indicator of the likely equilibrium state. In all cases, the final state is checked so that it satisfies the equilibrium conditions indicated in eqs. (2.8) for each pair of subsystems.

2.2.2 Nonlinear regression using neural networks

For the non-linear regression leading to the best FH parameters we have used the utility *nntool* embedded in Matlab[38], with the network type *generalised regression*, with the *spread constant* set to 1. The network consists of only two layers. The input layer reads an entire region of the phase diagram as an ordered vector with components of either 1 or 2 representing the number of phases in the case assigned to that particular vectorial component. The output layer contains three

neurons for the three corresponding FH parameters χ_{12}, χ_{13} and χ_{23}. We have observed no better fit when three or more layers are used.

In the case of pH 5 we have numerically generated an ordered vector of only 53 components out of the experimental 101, which correspond to all the one (L) and two phase ($L + S$) systems and excludes the region where three phases ($L_1 + L_2 + S$) are experimentally found. In addition to these 53 cases, we have provided a number of additional points for the binary systems gelatin-water (8 points) and maltodextrin-water (8 points) to enhance the description of the phase boundary in the dilute region of one of the components, as we know *a priori* that both gelatin and maltodextrin are completely soluble over all the range of experimental compositions at the selected temperature. The addition of the binary system points thus defines the phase boundary in the regions of very dilute composition of either the component 2 or 3. Hence, the final input vector contained 69 components.

Moreover, the phase boundary predicted by the Flory-Huggins model with constant parameters for this ternary system is convex. However, in the experimental data at low concentrations of both gelatin and maltodextrin, a concave phase boundary with a bulge is observed. Thermodynamically, this bulge indicates the existence of two critical points which we believe to be unlikely. The most plausible situation is, instead, that some of the one-phase points found experimentally near the critical point might be in fact kinetically arrested two-phase dispersions with no visible phase separation. This is due to the fact that the thermodynamic forces leading to the phase separation are small there. Thus, even after the stated experimental waiting time for phase separation, these genuinely two phase systems may still look as if they were one phase. Thus, to complete our theoretical analysis, we have restored the convex form of the phase boundary by assuming that the three experimental points indexed as 49, 51 and 53 in table S2 (in the Supporting Information) are in reality two-phase systems instead of one-phase as initially proposed by the experiments. Our hypothesis is that these two-phase systems occurring at low polymer concentrations might have not show visible phase separation because of their very slow kinetics of nucleation and, thus, they might be experimentally observed as homogeneous mixtures.

As far as the training of the NN is concerned, we have used a set of 10 complete numerically obtained phase diagrams for the case of pH 5. The parameters of the training set are given in the table S1 of the Supporting Information. Once the NN is trained, the experimental phase diagram is given as input and one obtains the suitable FH parameters as a result. We have checked the correctness of this fit by comparing the theoretical outcome for the phase concentrations with the few experimentally available estimates. The fact that the method is a regression method assures that all the relevant information is used to set the parameters. Therefore, the overall fitness of the regression over the boundary line is a strong

indication that the predicted concentrations of the phases are also well described, within the uncertainties of the experimental information.

In the case of pH $3-4$ the input vector has 80 components and we have generated 12 sets of numerical experiments for the training (see table S4 in the supporting information). For this case one single set of FH parameters seems to be sufficient to describe the entire experimental phase diagram.

2.2.3 Tie-lines and calculation of the phase boundary

With the fitted FH parameters, the minimisation of the free energy from the model, using the methodology described above, allows us to calculate the concentrations of the pair of (homogeneous) phases in equilibrium for each experimental point, or for any general initial composition. The *loci* of the positions of the points representing the phases in equilibrium in a two-dimensional plot $(\phi_2, \phi 3)$, like in Figure 2.1, is a plot of the phase boundary predicted by the model.

2.3 Experimental studies of phase behavior

2.3.1 Materials and Methods

Materials

Both gelatin and maltodextin were supplied by Sigma-Aldrich (Spain). Type B Gelatin (CAS number 9000-70-8), with approximately a 74% protein content 50-100 kDa molecular weight and a gel strength around 225 g Bloom, was from bovine skin. This gelatin has its isoelectric point at pH$\simeq$ 5 [37]. Maltodextrin (CAS number 9050-36-6) is a nonionic polysaccharide obtained by partial hydrolysis of starch, and thus, it mainly consists of linear chains of D-glucose units connected by $\alpha(1\rightarrow 4)$ glycosidic bonds. The sample used in this work had a medium chain length, with 3.6 kDa molecular weight. . The amount of reducing sugars, expressed as the dextrose equivalent, was between 4-7%. Acetic acid solutions were prepared by dilution of glacial acetic acid, also provided by Sigma-Aldrich. Water was always used after purification with a MilliQ Synergy Smart UV water purification system, ensuring a resistivity at 25°C around 18 $M\Omega$·cm, and a conductivity around 0.06 μS/cm.

Since the Flory-Huggins model is given in terms of the volume fractions, we have to convert the original weight fractions into these former variables. We have obtained the densities of both polymers from the experimental determination of the overall densities of different aqueous solutions with known mass fractions, for

	ρ (pH 5) g/cm^3	ρ (pH 3-4) g/cm^3
Gelatin	1.37	1.28
Maltodextrin	1.45	1.39
Water	0.99	
Water+ Acetic acid		0.99

Table 2.1: Estimated densities ρ of maltodextrin, gelatin and water in solution.

both pH conditions. We have then made a linear regression of the data to obtain the densities of the polymers in solution, which are shown in Table 2.1.

The volume fractions are then obtained according to the expression

$$\phi_i = \frac{w_i/\rho_i}{\sum_{j=1}^{3} w_j/\rho_j} \tag{2.1}$$

For $i = 1, 2, 3$, corresponding to water, gelatin and maltodextrin, respectively.

Experimental determination of phase diagrams

The phase behavior of gelatin and maltodextrin aqueous mixtures was studied at two different pH values, either at pH 5, by dissolving the two polymers in purified water, or in acidic conditions at pH values between 3 and 4, depending on the gelatine/acetic acid ratio, by dissolving the two biopolymers in constant concentration of acetic acid. Considering that the isoelectric point of type B bovine gelatin is around pH $5 - 7$, it is well below its isoelectric point, in the presence of acetic acid, ensuring that the molecules are highly negatively charged.

First, 25 wt% gelatin stock solutions were prepared by dispersing gelatin into warm water at 60°C while stirring during 30 min. Additionally, 30 wt% maltodextrin stock solutions were prepared by stirring the mixture at 95°C in hot water during 30 min, in tightly sealed glass vials to avoid evaporation of water. These stock solutions were preserved in a refrigerator at $\simeq 4$°C, taking into account that the maltodextrin has low solubility at room temperature and gelatin solutions become gelified below approximately 30°C. Stock solutions thus required reheating at 60°C, while applying gentle agitation, until low-viscosity homogeneous mixtures were recovered before their use.

All samples for phase behavior observations were prepared by mixing given amounts of the gelatin and the maltodextrin stock solutions, at 50°C, with the appropriate amount of purified water. We prepared samples that contained gelatin at concentrations ranging between $0 - 12$ wt%, and maltodextrin between $0 - 22$ wt%. These samples were prepared in 5 mL glass vials and filled up to a

total weight of 4 g by adding first water and then the appropriate amounts of maltodextrin and gelatin solutions. Then, vortex agitation was applied during 10 seconds and the closed vials were placed into a thermostated bath at 50°C constant temperature. The resulting phase behavior was observed after waiting a minimum of 5 days. This equilibration time was selected because phase separation in this system is relatively slow and requires a rather long time to observe phase changes visible to the naked eye. The equilibration time was not extended to longer periods, however, to prevent possible thermal degradation of gelatin under these conditions.

2.3.2 Raman determinations

Raman spectroscopy was used to qualitatively analyse a solid-like sediment that formed in many samples after equilibration for 5 days at 50°C. These sediments were extracted using pipettes, from the bottom of vials, and were placed on a petri dish where excess liquids were removed by contact with filter paper. Then, samples were dried and ground before placing them into the sample holder of the Raman spectrophotometry apparatus. Washing the sediment with water was not performed, to prevent gelatin removal due to its high solubility.

A micro-Raman, Jobin-Yvon LabRam HR 800, dispersive spectrometer was used coupled to an Olympus BXFM optical microscope, which was operated at 50x and 100x objective magnifications. The detection system was a CCD camera cooled to -70°C. The laser had a wavelength of 532 nm, with a power of $0.5 - 4$ mW, scanning at 600 lines/mm.

2.3.3 Quantification of phase separation by NIR transmittance

Phase separation and its velocity were analysed by measuring transmittance of Near Infrared Radiation (NIR), at different sample regions, as a function of time. For this purpose, a Turbiscan apparatus (Formulaction, France) was used (880 nm wavelength), with samples thermostated at 50°C.

2.4 Results and discussion

2.4.1 Phase behavior of gelatin/maltodextrin mixtures at both pH 5 and pH 3−4 (near and below the isoelectric point of gelatin, respectively).

Although the phase diagram of H_2O/gelatin/maltodextrin at pH 5 shows a similar behavior as previously reported [19, 39, 40, 41, 42], we observe some differences in the location of the phase boundaries. Some authors reported the phase boundary between two $(L+S)$ and three (L_1+L_2+S) phases at either lower concentrations [39, 40, 41] or higher concentrations [19] in comparison with the present work. Obviously, both gelatin and maltodextrin are natural products with a wide variability in their physicochemical properties (chain length and molecular weight, isoelectric point, charge density, etc.). Consequently, samples extracted from different sources and batches may have different properties, which produce variations in their phase behavior.

The experimental phase diagrams for the two conditions studied in this article are shown in Figure 2.1. At pH 5 (Figure 2.1a), three different scenarios are observed, depending on the total sample composition. At low concentrations of both gelatin and maltodextrin, one single phase (L) is observed, indicating a perfect miscibility of gelatin and maltodextrin. However, at slightly higher concentrations a liquid supernatant coexists with a denser solid-like precipitate $(L+S)$, which can be easily observed at the sample bottom by the naked eye. Herein, such a precipitate will be denoted as a solid phase (S). Above a certain concentration threshold, phase separation within the liquid phase also occurs. Three equilibrium phases are then observed, consisting of two liquid phases plus a solid (L_1+L_2+S), whose nature may be different from the previously referred one. Figure 2.2 shows an example of a sample containing the three phases.

The phase diagram at pH $3-4$ (Figure 2.1b) follows a different pattern. In this latter case, no three-phase region is observed among the experimentally studied points.

2.4.2 Analysis of the pH 5 case

The experimental evidence of a complex phase diagram for this case suggests that important microscopic changes take place, mostly due to the electrolytic nature of gelatin. Thus, aiming at constructing a model with predictive capacity, but

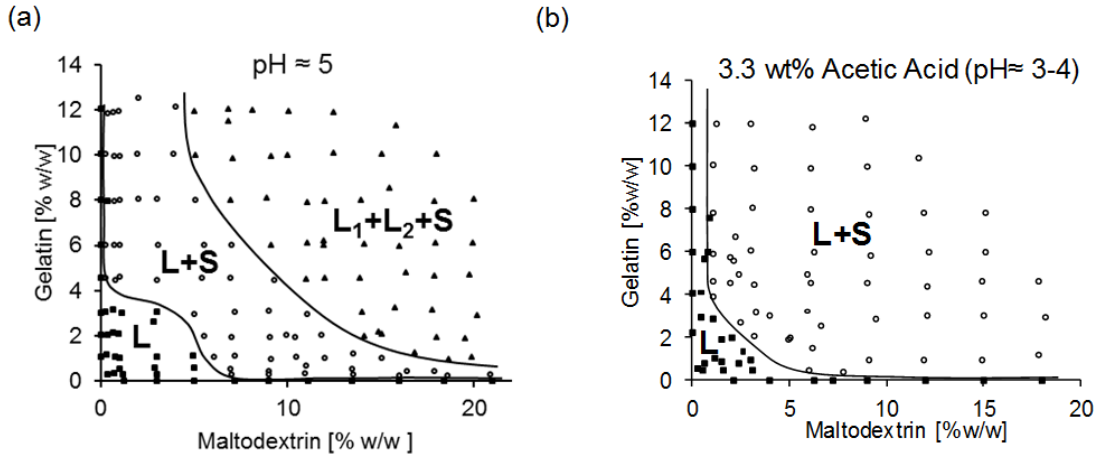

Figure 2.1: Experimental phase diagrams of the H_2O/gelatin/maltodextrin ternary system as a function of maltodextrin and gelatin concentrations, observed at 50°C after 5 days of equilibration. All tested compositions are shown, and the boundary lines were drawn, separating data points that showed a different phase behavior. The precision of these boundary lines is given by the distance between the neighboring points. (a) Phase diagram at pH 5, prepared with purified water. Three different regions are indicated: a homogeneous liquid solution (L), observed at low concentrations, a second region where the liquid phase coexists with a solid precipitate ($L + S$), and a third region observed at high concentrations where two equilibrium liquid phases coexist with a solid phase ($L_1 + L_2 + S$). (b) Phase diagram in the presence of constant 3.3 wt% acetic acid with pH $3 - 4$ (pH varies depending on gelatin concentration). At such acidic conditions, only (L) and ($L + S$) regions were observed. (The phase diagram at pH5 has been reproduced from a previous work [17], with permission of the American Chemical Society).

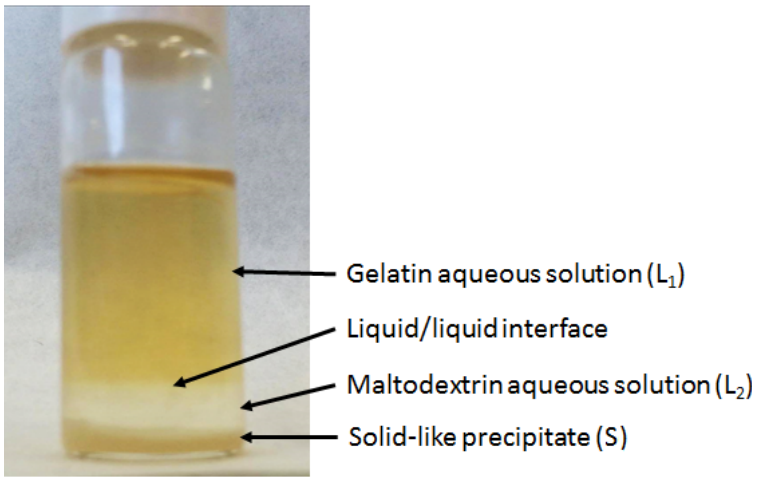

Figure 2.2: Example of a three phase separation ($L_1 + L_2 + S$) at pH 5 after 5 days at 50°C. The lower density phase (L_1) is a gelatin-rich aqueous solution; the intermediate phase (L_2) is a maltodextrin-rich solution and the denser phase (S) had a solid-like appearance, resembling a coacervate.

simple enough to be useful, some decisions have to be taken. In the first place, the observation that the third solid-like phase is dynamically produced at the liquid-liquid interface is indicative of the occurrence of significant conformation changes on contact between the two species. A theory such as Flory Huggins with constant parameters cannot account for such a behavior. Hence, we have excluded the information related to the three phase region in the training of the NN, and concentrated only on the behavior of the most relevant regions for the nanogel formation, namely those of one and two phases.

The experimentally reported bulge in the region of the one phase systems indicates that the phase-boundary would be concave there, instead of the convex form observed in the rest of the diagram. Such an anomalous curvature has not been observed in previous experimental studies [19]. It is plausible then that some of the points identified as one-phase points are in fact two-phase points. As mentioned before, these compositions are close to the critical point, where the time for the phase separation increases as the thermodynamic force for the phase separation weakens. For the sake of simplicity in the interpretation of the results, we will assume for the rest of the article that the phase diagram has one single critical point and that some of the experimental points for pH 5 are not truly at equilibrium.

The parameters used to create the training set are given in Table S1 (*cf.* Supporting Information). The FH parameters of our best fit are given in Table 2.2.

	χ_{12}	χ_{13}	χ_{23}
Best fit FH parameters for pH 5	0.1012	0.6988	1.2071

Table 2.2: Proposed Flory-Huggins parameters for the gelatin-maltodextrin aqueous mixture after the neural network regression. In this work χ_{12} stands for the FH water-gelatin interaction parameter, while χ_{13} is the water-maltodextrin and χ_{23}, the gelatin-maltodextrin.

These calculated FH parameters are consistent with what can be expected from the known solubilities of gelatin and maltodextrin in water. Indeed, χ_{12} has a low value corresponding to a high hydrophilicity of gelatin, whereas a larger χ_{13} can be related to a lower water solubility of maltodextrin. Notice that the value of the FH parameter χ_{13} given in Table 2.2, although larger than $1/2$, is still smaller than the critical FH parameter $\chi_{13}^c \simeq 0.74$, due to the small size of this polymer. This fact indicates that the model is able to correctly predict the full solubility of maltodextrin as a binary mixture with water. Finally, χ_{23} is the largest of the FH parameters, suggesting that the interaction between gelatin and maltodextrin monomers is very repulsive. Hence, the addition of maltodextrin in a gelatin aqueous solution and viceversa will produce a reduction of the overall solubility of each of the polymers, ultimately producing a phase separation.

Once the parameters have been fitted, we can numerically reproduce the phase diagram, including the boundary line between the L and the $L+S$ regions, following the methodology sketched in 2.2.3. In Figure 2.3 we show the phase diagram and the tielines for the system at this pH. One can observe that the numerical phase boundary lies very close to the experimental one. It should be remarked that this good agreement has been achieved without including the electrolytic nature of gelatin and in the absence of experimental information about the compositions of the phases.

In the Supporting Information we provide the compositions of all the phases in equilibrium corresponding to the experimental state points connected by tielines, as obtained from the optimal FH model. Our calculation indicates that the critical point for the $L+S$ separation is located around 0.01 gelatin and 0.02 maltodextrin volume fractions. This critical point has not been reported in the literature, to the best of our knowledge, because of its difficult experimental determination, but also because previous experimental work has focussed mainly on the L_1+L_2 phase separation.

Experimentally, the visual aspect of the solid precipitate, S, was similar in both the $L+S$ and L_1+L_2+S regions of the phase diagram. In the two phase region $(L+S)$, the precipitate seemed to continuously form until equilibrium was reached

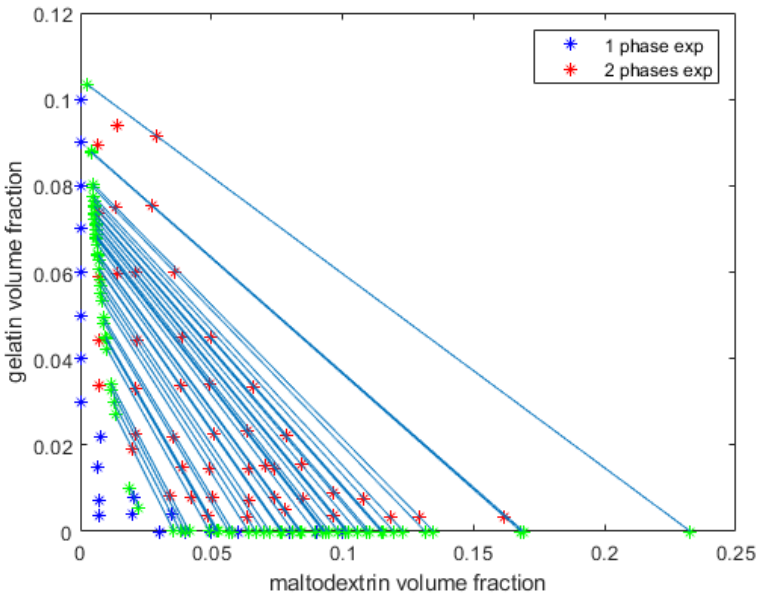

Figure 2.3: Comparison between the experimental and the theoretically predicted phase diagram for the case of pH 5 using the best fit of FH parameters (*c.f.* Table 2.2). The boundary lines between homogeneous liquid mixtures (L) and two-phase systems with solid-like precipitate ($L+S$) are also shown. Blue lines are the numerically calculated tielines. The numerical compositions related to the tielines are given in Table S2 in the Supporting Information.

after around 5 days, while keeping a constant temperature of 50°C. This behavior in the gelatin-maltodextrin system was previously reported by other authors [19, 42]. The solid sediment was analysed by optical rotation and NMR [19], which showed that this precipitate was enriched in longer and more branched maltodextrin molecules, while shorter and more linear maltodextrin chains tended to remain in the liquid phase in larger numbers. In the present work small amounts of gelatin were detected in the solid, but it was mainly attributed to cross-contamination during extraction of the precipitate, particularly in the samples containing large amounts of gelatin, forming a small volume of maltodextrin precipitate. This interpretation is consistent with the numerical calculations using the fitted FH parameters. Consequently, it was inferred that since maltodextrin is a natural product with high polydispersity and branching, the different species segregate, each according to their solubility in the presence of gelatin. Moreover, it has been found that the weight of sedimented solid, obtained within the $L + S$ region of the phase diagram, varies with both gelatin and maltodextrin concentrations [19] following the empirical expression $M = K[\text{Maltodextrin}]^2[\text{gelatin}]$. In more recent studies [42], it has been demonstrated that maltodextrin can undergo a transition from disordered random coils to aggregated rigid helices, which are significantly less soluble in water. This transition can be caused by the presence of ionic molecules, such as gelatin.

In the case of solid formation within the three-phase region ($L_1 + L_2 + S$), by visual inspection by the naked eye, we have observed that the precipitate forms first in the two-liquid interfacial region between a gelatin-rich and maltodextrin-rich aqueous solutions, while the precipitate, located at the bottom of the sample, only becomes visible later on. These visual observations were confirmed by measuring light transmission across the sample vial and at different positions along the vertical axis, using a Turbiscan apparatus operated at 50°C (results included as supporting information, Fig. $S1$). The results showed that initially transmission decreases at the interface between the two liquid phases L_1 and L_2 due to the forming precipitate. The transmission there later increases while simultaneously strongly decreases near the bottom of the vial, due to the accumulation of the precipitate on the glass surface due to sedimentation. Therefore, in the three-phase region the formation of the precipitate at the interface between the two phases could be caused by a structural change in maltodextrin, which would make the solid form by nucleation at the interfacial region, where gelatin and maltodextrin are in contact and in high concentrations.

As was already mentioned, such an observed behavior cannot be explained in terms of a simple phase separation from a mixture of components without structural properties. Following the conjectures inferred from the experimental observations within the three-phase region, we can explain the formation of the solid

pH 5 case								
	av. composition				L phase		S phase	
	$w_2\%$	$w_3\%$	$\overline{\phi}_2$	$\overline{\phi}_3$	ϕ_2	ϕ_3	ϕ_2	ϕ_3
a	12	5	0.0910	0.0358	0.1058	0.0026	$< 10^{-4}$	0.2407
b	5	12	0.0380	0.0863				
c	3	16	0.0230	0.1159				
d	3	20	0.0233	0.1469				

Table 2.3: Compositions corresponding to the states where the Raman spectroscopy of the precipitate has been performed. Phases L, S are the lightest and the heaviest, respectively. Points with three phases ($L_1 + L_2 + S$) do not have a numerical evaluation of their compositions.

phase as a consequence of conformational changes in the maltodextrin caused by the presence of gelatin along with the counter ions entrained by the latter. Therefore, from a thermodynamic viewpoint, maltodextrin in either one or the other conformations should be treated as separate species. Such a treatment cannot be achieved with the available experimental information and is beyond the scope of the present work. The Flory-Huggins parameters given in Table 2.2 correspond to the interaction of the presumed globular maltodextrin with water and gelatin. This reason justifies our decision to exclude the analysis of the three-phase cases in the fit of the model parameters for this system.

Using Raman spectroscopy as indicated in Sec. *Raman determinations*, we have qualitatively determined the composition of the phase at the bottom of the vial for the four different cases specified in Table 2.3. In particular, case a lies in the $L+S$ two-phase region while cases b, c and d are within the L_1+L_2+S three-phase region. In Figure 3.8 we show the spectra obtained after the analysis of the precipitate in the aforementioned states and in comparison with the ones of pure maltodextrin and gelatin. Clearly, the precipitate in cases b, c and d is maltodextrin, and, therefore, the precipitate in the three phase region is predominantly maltodextrin. However, for case a Raman spectroscopy clearly shows an important presence of gelatin in the maltodextrin, contrary to the common belief that the precipitate is mostly maltodextrin. We should point out that the *heaviest* phase is the one with highest mass density ρ, which can be estimated as

$$\rho = \rho_1\phi_1 + \rho_2\phi_2 + \rho_3\phi_3 \tag{2.1}$$

The numerical estimate of the heaviest phase, S, of case a is $\rho_c = 1,10$ g/cm^3, while the dilute phase has a mass density $\rho_d = 1,03$ g/cm^3. This difference is

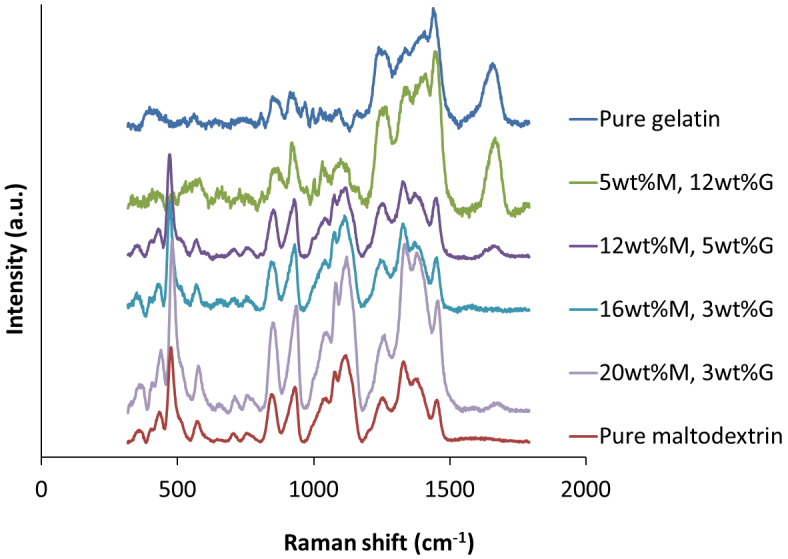

Figure 2.4: Raman spectra for different test compositions in the pH 5 case, of the S phase, formed in $L_1 + L_2 + S$ situations.

sufficiently significant as not to be attributed to any uncertainty in the estimates. Hence, the presence of gelatin in the sample may be caused by cross contamination due to the small amount of the precipitate in this particular case.

2.4.3 Analysis of the pH 3-4 case

The presence of slight acidic conditions, below the isoelectric point of gelatin (I.P.$\simeq$ 5) alters the overall interactions between the species with the solvent and with themselves. At these acidic conditions, the coexisting two-liquid phases are not found, and the only phase boundary is the one between a liquid in equilibrium with a solid-like precipitate. Therefore, we should provide a new set of FH parameters that adequately describe the observed phase diagram for the new conditions. Contrary to pH 5, for this system the phase boundary experimentally found is convex and shows no anomalous behavior and all the experimental points can be used in the fit. A training ensemble containing only 12 sets of states is employed. The parameters describing the training set are given in Table S4. The regression by means of the NN yields the best fit of FH parameters for the experimental phase diagram, which are given in Table 2.4. The acidic conditions reduce the repulsive interactions between the species and, as a consequence, the phase diagram is reasonably well described with a single set of FH paramenters, together with the fact

	χ_{12}	χ_{13}	χ_{23}
Best fit FH parameters	0.296	0.560	1.090

Table 2.4: Best fit for the FH parameters for the pH 3-4 case as found from the regression.

that no three-phase region is observed under acidic conditions, in agreement with the experimental observations. As before, these fitted parameters permit us to calculate the phase diagram together with the compositions of each phase at each of the 80 states where we have experimental data. The comparison between both is given in Figure 3.10. As can be seen in Figure 3.10, by the differences in the experimental and numerical phase boundaries, there are only 11 points where there is a disagreement. Although the concentration dependence of the FH parameters seems to be weaker for these acidic conditions, still this disagreement suggests that a better model could be obtained if this dependence is taken into consideration.

To further check the quality of the prediction, we have conducted Raman spectroscopy, as already described. The predicted compositions at the selected points are given in Table 2.5, and the observed spectra are shown in Figure 2.6. The experimental evidence indicates that cases a and b are gelatin-rich precipitates while cases c and d are maltodextrin-rich. However, this observation should be considered with caution, since the extraction of the precipitate in gelatin-rich overall compositions is prone to cross-contamination with gelatin. In any case, the predictions of the model suggest that all four points should correspond to maltodextrin-rich precipitates, according to Table 2.5. Notice, however, that the differences in mass density between L and S phases is around 1%. Therefore, any inaccuracy in the determination of the densities of the polymers in solution, as well as the shift in the phase boundary obtained, can make a qualitative change in which of the phases is going to be found at the bottom of the vial, according to our numerical solution. What is indeed relevant is the fact that the difference in mass density between the phases continuously increases from a to d. Thus, if $\rho_2 = 1.37$ g/cm^3 and $\rho_3 = 1.40$ g/cm^3, for instance, were used instead of the actual values, then the predictions of the model would agree perfectly with the Raman spectroscopy. Therefore, we can conclude that the model developed for this acidic case also gives a physically consistent picture of the phase behavior.

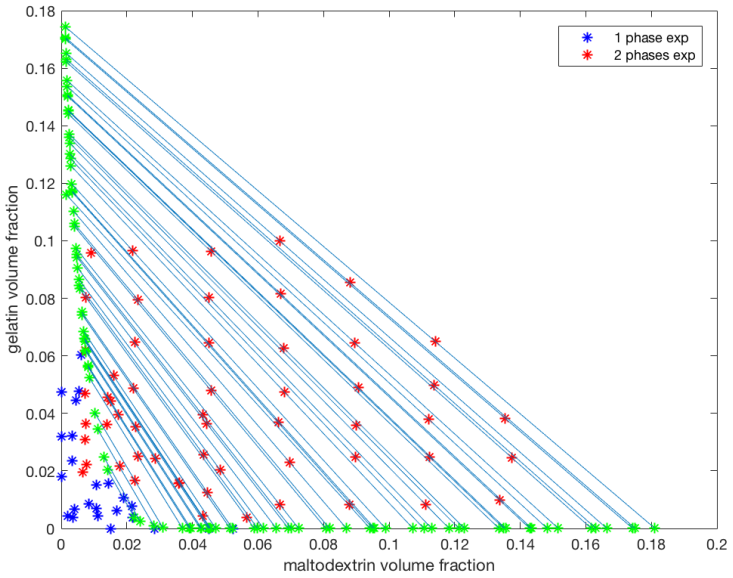

Figure 2.5: Phase diagram for the case of pH 3-4. Blue and red circles correspond to the experimental one and two phase regions, respectively. Blue and red crosses also indicate the predicted regions of one and two phases. The solid line shows an estimate of the experimental phase boundary, while the dashed line corresponds to the numerical estimate.

ph 3-4 case								
	av. composition				L phase			
	$w_2\%$	$w_3\%$	$\overline{\phi}_2$	$\overline{\phi}_3$	ϕ_2	ϕ_3	ρ	$\Delta\rho$
a	12	5	0.0970	0.0210	0.1363	0.0024	1.0320	0.0085
b	5	12	0.0410	0.0900	0.1394	0.0023	1.0329	0.0095
c	3	16	0.0250	0.1200	0.1506	0.0019	1.0359	0.0132
d	3	20	0.0250	0.1520	0.1722	0.0013	1.0419	0.0208

ph 3-4 case								
	av. composition				S phase			
	$w_2\%$	$w_3\%$	$\overline{\phi}_2$	$\overline{\phi}_3$	ϕ_2	ϕ_3	ρ	$\Delta\rho$
a	12	5	0.0970	0.0210	$< 10^{-6}$	0.1219	1.0406	0.0085
b	5	12	0.0410	0.0900	$< 10^{-6}$	0.1264	1.0424	0.0095
c	3	16	0.0250	0.1200	$< 10^{-6}$	0.1434	1.0492	0.0132
d	3	20	0.0250	0.1520	$< 10^{-6}$	0.1775	1.0628	0.0208

Table 2.5: Compositions corresponding to the states used for the Raman spectroscopy of the precipitate in the pH 3-4 case. The mass densities ρ are estimates and are given in units of g/cm^3. Phases L and S are ordered according to their mass density, from the lightest to the heaviest.

2.5 Conclusions

The analysis of the phase diagram of ternary solutions of gelatin, maltodextrin and water at 50° C is particularly relevant for the formation of water/water emulsions and gelatin microgels. Two different pH conditions have been studied, near and below the isoelectric point of gelatin, namely pH 5 and $3-4$, respectively. We experimentally found the approximate phase boundaries for spontaneous phase separation of the components into two or even three phases. The domain of overall concentrations leading to the two-phase region is of particular interest for the preparation of colloidal dispersions in gelatin/maltodextrin aqueous mixtures, with many potential applications in the formulation of food products, among others. Since maltodextrin is the soluble fraction of starch, and gelatin is a common protein used in food products, edible natural product, gelatin/maltodextrin aqueous mixtures can be used as a model system for food formulations. Our study of this system is particularly addressed to foster the development of new applications based on colloidal dispersions in gelatin/maltodextrin mixtures.

In this article we have also introduced a novel method to determine the optimal Flory-Huggins parameters based on a non-linear regression of the experimen-

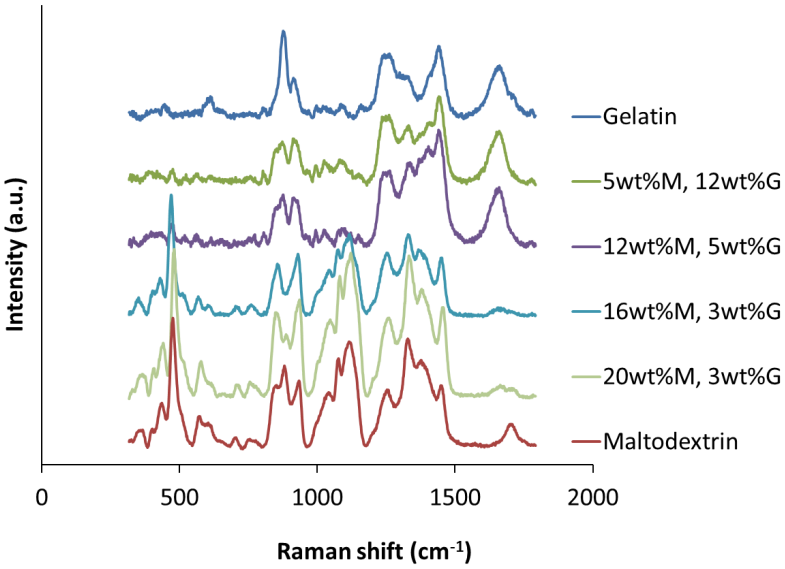

Figure 2.6: Raman spectra for different test compositions in the pH 3-4 case

tal phase diagram. We trained a neural network by providing only the number of phases for a large number of state points, generated from the FH model with arbitrary FH parameters. The experimental phase diagram, with no knowledge of the compositions of the coexisting phases at each state point, was then given to the network to produce the optimal parameters consistent with the phase diagram. Remarkably, this method is able to find a reasonable fit of the phase diagram, including reasonable estimates of their compositions at the experimental points. The method, however, requires the presence of phase boundaries in the experimental data to be used for the fit, due to the fact that the useful information lies precisely in the change in the number of phases across varying system compositions, if no other information is available. The quality of the results is, therefore, strongly bound to the quality with which such phase boundaries are reproduced by the model. Otherwise, the estimated concentrations of the phases cannot be relied on.

The combined experimental and numerical studies have the advantage of providing a physically sound perspective of the phase behavior of the analysed system. It is interesting to note that the mass densities of the phases in the pH 5 case are significantly different from each other so that the vertical ordering of the phases in the vial is unequivocally determined by the fitted model, and is in agreement with the experimental observations. However, in the analysis of the pH 3-4 case we have observed that the coexisting phases have similar densities, which makes the prediction of the vertical ordering in the vial sensitive to the actual polymer

densities in solution, for which we have only rough estimates. In any case, the predicted volume fractions still provide important information about the system itself, as we have discussed in view of the Raman spectroscopy results.

The analysis provided in this article is expected to be of great help in determining the optimal conditions for the formation of nanostructured systems based on phase separation of these two edible polymers. We have seen that changes in the pH can significantly modify the phase diagram, but also the overall composition of the coexisting phases, permiting different strategies for the formation of nanostructured materials. Future studies should address the kinetics of the phase separation to understand how to produce non-equilibrium structures by kinetically arresting the system at the early stages of the phase separation, if these thermodynamic conditions are well controlled, which is the main result of the present article.

Bibliography

[1] Beijerinck, MW. **Ueber eine Eigentümlichkeit der löslichen Stärke.** *Zentralblatt für Bakteriol Parasitenkd und Infekt.* **1896**, *2(22)*, 697-699.

[2] Kang, C.; Sandler, S. **Phase behavior of aqueous two-polymer systems.** *Fluid Phase Equilib.* **1987**, *38*, 245-272.

[3] Hatti-Kaul, R. **Aqueous Two-Phase Systems: A General Overview.** *Mol Biotechnol.* **2001**, *19*, 269-277.

[4] Esquena, J. **Water-in-water (W/W) emulsions.** *Curr Opin Colloid Interface Sci.* **2016**, *25*, 109-119. doi,10.1016/j.cocis.2016.09.010.

[5] Bütschli, **O. Untersuchungen über Strukturen: insbesondere über Strukturen nichtzelliger Erzeugnisse des Organismus und über ihre Beziehungen zu Strukturen, welche ausserhalb des Organismus entstehen.** *In: Leipzig: Verlag Von Wilhelm Engelmann*, **1898**, 251.

[6] Beijerinck, MW. **Ueber emulsionsbildung bei der vermischung wässeriger Lösungen gewisser gelatinierender kolloide.** *Zeitschr Chem Ind Kolloide (Kolloid Z).* **1910**, *7*,16.

[7] Wesslen, T.; Albertsson, P. A.; Philipson, L. **Concentration of animal viruses using two-phase systems of aqueous polymer solutions.** *Arch Gesamte Virusforsch.* **1959**, *9*, 510-520.

[8] Norrby, E.C.J.; Albertsson, PA. **Concentration of poliovirus by an aqueous polymer two-phase system.** *Nature.* **1960**, *188 (4755)*, 1047-1048.

[9] Albertsson, PA. **Partition of proteins in liquid polymer-polymer two-phase systems.** *Nature.* **1958**, *182*, 709-711.

[10] Hatti-Kaul, R. Ed. **Aqueous Phase Systems, Methods and Protocols.** *New Jersey: Methods Biotechnol. Vol. 11, Humana Press* **2000**.

[11] Grinberg, VY.; Tolstoguzov, VB. **Thermodynamic incompatibility of proteins and polysaccharides in solutions.** *Food Hydrocoll.* **1997**, *11(2)*, 145-158. doi:10.1016/S0268-005X(97)80024-0.

[12] Lorén, N.; Hermansson A. **Phase separation and gel formation in kinetically trapped gelatin/maltodextrin gels.** *Int J Biol.* **2000**, *27*, 249-262. http://www.sciencedirect.com/science/article/pii/S0141813000001276. Accessed December 22, 2014.

[13] Nawong, S.; Oonsivilai, R.; Boonkerd, N.; Truelstrup Hansen, L. **Entrapment in food-grade transglutaminase cross-linked gelatin-maltodextrin microspheres protects Lactobacillus spp. during exposure to simulated gastro-intestinal juices.** *Food Res Int.* **2016**, *85*, 191-199. doi:10.1016/j.foodres.2016.04.041.

[14] Kasapis, S.; Morris, E.R.; Norton, I.T.; Clark, A.H. **Phase equilibria and gelation in gelatin/maltodextrin systems — Part IV: composition-dependence of mixed-gel moduli.** *Carbohydr Polym.* **1993**, *21(4)*, 269-276. doi:10.1016/0144-8617(93)90058-C.

[15] Alevisopoulos, S.; Kasapis, S.; Abeysekera, R. **Formation of kinetically trapped gels in the maltodextrin—gelatin system.** *Carbohydr Res.* **1996**, *293(1)*, 79-99. doi:10.1016/0008-6215(96)00188-7.

[16] Kasapis, S.; Morris, E.R.; Norton, I.T.; Clark, A.H. **Phase equilibria and gelation in gelatin/maltodextrin systems — Part I: gelation of individual components.** *Carbohydr Polym.* **1993**, *21(4)*, 243-248. doi:10.1016/0144-8617(93)90055-9.

[17] Beldengrün, Y.; Aragon, J.; Prazeres, S.; Montalvo, G.; Miras, J.; Esquena, J. Gelatin-Maltodextrin **Water-in-Water (W/W) Emulsions for the Preparation of Crosslinked Enzyme-Loaded Microgels.** *Langmuir.* **2018**, *34*, 9731-9743.

[18] Djabourov M. **Architecture of gelatine Gels.** *contemporary Physics.* **1988**, *29*, 273-297.

[19] Kasapis, S.; Morris, E. R.; Norton, I. T.; Gidley, M. J. **Phase Equilibria and Gelation in Gelatin/Maltodextrin Systems — Part II: Polymer Incompatibility in Solution.** *Carbohydr. Polym.* **1993**, *21 (4)*, 249-259.

[20] Piculell, L.; Lindman, B. **Association and segregation in aqueous polymer/polymer, polymer/surfactant, and surfactant/surfactant mixtures: similarities and differences.** *Adv Colloid Interface Sci.* **1992**, *41*, 149-178.

[21] Kwak, J.C.T. ed. Polymer-Surfactant Systems. *New York: Marcel Dekker.* **1998** *77*,1.

[22] Lindman, B. **Surfactant-Polymer mixtures.** *In: Holmberg K, ed. Handbook of Applied Surface and Colloid Chemistry, Vol. 1. Chichester, UK: John Wiley & Sons, Inc.* **2002**, 445-464.

[23] Jönsson, B.; Lindman, B.; Holmberg, K.; Kronberg, B. **Surfactants and Polymers in Aqueous Solution.** *In: Chichester, UK: John Wiley & Sons, Inc.* **1999**, 219-246.

[24] Flory, P.J. **Principles of Polymer Chemistry.** *New York: Cornell University Press*, **1953**.

[25] Flory, P.J.; Krigbaum, W.R.; **Thermodynamics of High Polymer Solutions.** *Annu Rev Phys Chem.*, **1951**, *2(1)*, 383-402. doi:10.1146/annurev.pc.02.100151.002123.

[26] Huggins, M.L. **Theory of Solutions of High Polymers.** *J Am Chem Soc.* **1942**, *64(7)*, 1712-1719. doi:10.1021/ja01259a068.

[27] Burchard, W. **Solution Thermodynamics of Non-Ionic Water Soluble Polymers.** *In: Finch C, ed. Chemistry and Technolgy of Water-Soluble Polymers. Springer.* **1983**, 125-142.

[28] Johansson, H.O.; Karlström, G.; Tjerneld, F.; Haynes, C. A. **Driving forces for phase separation and partitioning in aqueous two-phase systems.** *J Chromatogr B Biomed Sci Appl.* **1998**, *711(1-2)*, 3-17. doi:10.1016/S0378-4347(97)00585-9.

[29] Schmitt, C.; Sanchez, C.; Desobry-Banon, S.; Hardy, J. **Structure and technofunctional properties of protein-polysaccharide complexes: a review.** *Crit Rev Food Sci Nutr.* **1998**, *38(8)*, 689-753. doi:10.1080/10408699891274354.

[30] Horst, R. B.A. W. **Thermodynamics of polymer solutions. 2016**.

[31] Prausnitz, J.M; Lichtenthaler, R.N.; Gómez de Azevedo, E.; **Molecular Thermodynamics of Fluid-Phase Equilibria.** *Prentice Hall PTR, New Jersey.* **1999**.

[32] Clark, A.H. **Direct analysis of experimental tie line data (two polymer-one solvent systems) using Flory-Huggins theory.** *Carbohydr Polym.* **2000**, *42(4)*, 337-351. doi:10.1016/S0144-8617(99)00180-0.

[33] Elias, H.J. **Macromoleules.** *Weinheim:John Wiley-VCH Verlag cop.* **2005-2009**.

[34] Quian, C.S.; Mumby, S.J.; Eichinger, B.E. **Existence of 2 critical concentrations in binary phase-diagrams.** *J. Polym. Sci., Part B: Polymer Physics,* , **1991**, *29*, 635.

[35] Quian, C.S.; Mumby, S.J.; Eichinger, B.E. **Phase-diagrams of binary polymer-solutions and blends.** *Macromolecules.* **1991**, *24*, 1655.

[36] Panagiotopoulos, A.Z.; **Direct determination of phase coexistence properties of fluids by Monte Carlo simulation in a new ensemble.** *Molecular Physics.* **1987**, *61*, 813-826.

[37] Raja Mohd Hafidz, R.N.; Yaakob, C.M.; Amin, I.; Noorfaizan, A.; **Chemical and functional properties of bovine and porcine skin gelatin**, *International Food Research Journal*, **2011** *18*, 813-817.

[38] **Deep Learning Toolbox, MATLAB version 9.2.0.556344 (R2017a)**. *The MathWorks Inc. Natick, Massachusetts* **2017**.

[39] Aymard, P.; Williams, M. A. K.; Clark, A. H; Norton, I. T. A **Turbidimetric Study of Phase Separating Biopolymer Mixtures during Thermal Ramping.** *Langmuir.* **2000**, *16*, 7383-7391.

[40] Norton, I. T.; Frith, W. J. **Microstructure Design in Mixed Biopolymer Composites.** *Food Hydrocolloids.* **2001**, *15*, 543-553.

[41] Khan, R. S.; Nickerson, M. T.; Paulson, A. T.; Rousseau, D. **Release of Fluorescent Markers from Phase-Separated Gelatin-Maltodextrin Hydrogels.** *J. Appl. Polym. Sci.* **2011**, *121*, 2662-2673.

[42] Hoey, A.; Ryan, J. T.; Fitzsimons, S. M.; Morris, E. R. Segregative **Interactions in Single-Phase Mixtures of Gelling (Potato) Maltodextrin with Other Hydrocolloids.** *Gums and Stabilisers for the Food Industry, in*

P.A., Williams and G.O., Philips (eds.). The proceeding of the 18th gums and stabilisers for the food industry: Hydrocolloid functionality for affordable and sustainable global food solutions. Royal Society of Chemistry. **2016**. 305.

Chapter 3

Folding Domain Functions: a Random Variable Transformation technique for the non-invertible case, with applications to REDs

To Roberto Blanchini, in memoriam

3.1 Introduction

The theory of random dynamical systems has been greatly developed in the past fifty years, both from the theoretical and applied point of view [2, 3]. Particularly relevant are the applications to biology, economics and social sciences. More recent applications involve models related to problems in climatology, combustion theory and conduction of electrical impulses in nerve axons [1], just to mention a few examples and to show the great deal of interest in this area of research.

The more general models involve the study of a random differential equations with random initial data, along with the effect of time-dependent noise sources. However, there are many significant examples where such time-dependent noise sources are not present. In these cases, one deals with a deterministic (non-random) law describing the dynamic evolution of the model, where the probabilistic effects only concern the randomness of the initial conditions. In this situation, we can model the dynamic phenomenon as a map which transforms random initial conditions, expressed by a random variable (RV), to an output, whose probability distribution is to be determined [5, Ch.5]. Problems of this kind can be theoretically settled within the framework of the theory of functions of a random variable.

More in detail, let X be a random variable, with density function μ_X, defined on a probability space $\Omega = (\Omega, \mathcal{A}, p)$, [1] with values into $\mathbb{R}$, and let g be a real function defined on $\mathbb{R}$, which may require some properties that we discuss later on. A classical problem considered in the literature consists in determining the probability distribution of $Y = g(X)$ from the information about X and g. This problem is solved by a standard procedure, by assuming g to be invertible (see [4, p.81]). In particular, in the one-dimensional case, $g : \mathbb{R} \to \mathbb{R}$, we have a precise formula for the density function μ_Y of Y provided that g is continuously differentiable with a non-vanishing first derivative [4, Corollary 11.2]. A more complex situation arises if g is only piecewise strictly monotone, but continuously differentiable, with a finite set of isolated points where the derivative vanishes, which is the problem that we address in the present article. In this case, if $I_1, \ldots, I_n$ is a finite sequence of intervals decomposing the domain of g and such that g is strictly monotone and continuously differentiable in the interior of each interval, we have that

$$\mu_Y(y) = \sum_{i=1}^{n} \mu_X(h_i(y))|h_i'(y)|\mathtt{1}_{\wedge}(y), \tag{3.1}$$

where h_i is the inverse function of g but restricted to the interval I_i, $\wedge = \{y : y = g(x) : x \in \mathbb{R}\}$ and $\mathtt{1}_{\wedge}(y)$ is the characteristic function which takes a value 1 on $\wedge$ and 0 otherwise (see [4, Corollary 11.3]). Although the formula (3.1) provides a precise definition of the density function associated with the random variable Y, its implementation in concrete examples can be very difficult. Recent articles applying this method, named *Random Variable Transformation technique*, to different models of present interest in mathematical biology and population dynamics, for instance, deals with more specific situations when g is monotone on its whole domain or has a quadratic shape, thus reducing the complexity only to two symmetric intervals of invertibility (see [6, 7, 10, 9, 8] and the references therein). The aim of this article is precisely to provide the framework to build an efficient algorithm for these cases of interest that cannot be straightforwardly addressed within the standard approach.

A few typical cases, in which a function of a RV may occur in dynamical systems, are the following.

a) As a first example, let us consider the case of a discrete Dynamical System defined by a difference equation of the form

$$x_{n+1} = L(x_n), \tag{3.2}$$

[1] As usual, $\mathcal{A}$ denotes a σ-algebra of measurable sets (in the case of our applications $\mathcal{A}$ will denote the collection of Lebesgue measurable sets in $\mathbb{R}$) and p is a probability defined on $\mathcal{A}$.

with $L : A \to A$, where A is a suitable domain in $\mathbb{R}^d$ and L is a sufficiently smooth function. Typical models in population dynamics may involve a non-invertible map L, due to the presence of natural growth restrictions, for instance, of logistic type limitations [12]. The situation becomes even more complicated when we look for periodic points, a problem which is equivalent to the study of fixed points for iterates of L. For a non-invertible L, the shape of the k-th iterate $L^k = \underbrace{L \circ \cdots \circ L}_{k \text{ times}}$ can be extremely far from a monotone function. This is apparent even when studying one-dimensional classical logistic equations (see [11]), as shown in Figure 3.1 where the logistic map, together with its third iterate, is considered.

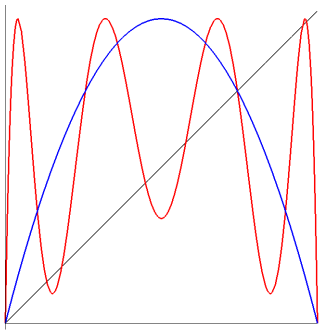

Figure 3.1: The figure represents the graph of the logistic map $L(x) = rx(1-x)$ and its third iterate $L(L(L(x))$ in the interval $[0, 1]$. For our example, we have considered the case $r = 3.9$ where there are points of (minimal) period three, as seen from the intersections with the line $y = x$, which is known to yield chaotic dynamics, according to [11].

If we assume that the initial point $x_0 := \phi$ is represented by a RV, we are interested in determining the probability distribution that describes the state of the system after a certain number k of iterates, or, equivalently, the probabilistic outcome at the k-generation.

b) As a second example, we consider the case of a continuous dynamical system associated with an ordinary differential equation. Here, we are interested in the particular case of a vector system ordinary differential equations of the form,

$$\begin{cases} \frac{d}{dt}\underline{x}(t) = \vec{f}\big(\underline{x}(t), t\big) \\ \underline{x}(t_0) = (x_1^0, x_2^0, \ldots, x_i^0, \ldots x_d^0) \end{cases} \tag{3.3}$$

where $\underline{x}(t) \in \mathbb{R}^d$. Let us assume that the initial condition $\underline{x}(t_0)$ contains one component, x_r, say, which is a RV, i.e. $x_r^0 = \phi$. If, for a moment, we suppose that

$\underline{x}(t_0)$ is a given specific a vector under natural regularity assumptions [13] on $\vec{f}$, we know that there is a unique solution $\varphi_{\underline{x}(t_0)}(t)$ defined on a maximal interval of existence. Suppose also that for a fixed interval $[t_0, t_1]$, $t_1 > t_0$, all the solutions with initial value $\underline{x}(t_0)$ in a given set D, are defined. In this case, the map $\Psi : \underline{x}(t_0) \mapsto \varphi_{\underline{x}(t_0)}(t_1)$ (the so-called Poincaré map) is a homeomorphism of D onto $\Psi(D)$, as it is well known in the theory of Dynamical Systems. Therefore, if $\underline{x}(t_0) = \phi \in \mathbb{R}$ (i.e. in the one-dimensional case), the map Ψ must be a strictly monotone function, and the RVT method can be straightforwardly applied. However, in all the other situations in which $d > 1$, which are also relevant in Physics, the monotonicity of the maps associated to Ψ is lost.

A significant example comes from the *shooting method*. In this case, we study a second-order scalar differential equation of Newtonian type of the form

$$y''(t) + f\big(y(t), y'(t), t\big) = 0, \tag{3.4}$$

corresponding to the planar system

$$\begin{cases} y'(t) = v(t) \\ v'(t) = -f\big(y(t), v(t), t\big). \end{cases} \tag{3.5}$$

The initial condition

$$y(t_0) = a,\ y'(t_0) = b,$$

reads now as

$$y(t_0) = a,\ v(t_0) = b.$$

Then, to the pair $(a, b) \in \mathbb{R}^2$, we associate the point

$$(a_1, b_1) := \varphi_{(a,b)}(t_1) = \big(\varphi^{(1)}_{(a,b)}(t_1), \varphi^{(2)}_{(a,b)}(t_1)\big) \in \mathbb{R}^2,$$

by means of the two-dimensional Poincaré map. Suppose now that for the initial pair (a, b) one of the parameters is determined (for instance the initial position a of the particle), while the other (for instance the initial velocity b) is a RV. In this case, we set $b = \phi$ and, instead of being interested in the complete map $\varphi_{(a,b)}(t_1)$, we restrict ourselves to the map which associates to ϕ the final position, $\varphi^{(1)}_{(a,\phi)}(t_1)$; this map is not invertible.

In the deterministic case, this procedure consists of fixing the initial position ϕ and look for the final one, given the initial velocity, which needs to be known at the beginning. Then, the probability distribution μ_Y can be reconstructed by *shooting* a bundle of trajectories by varying ϕ, and measuring the density of the end points $y(t)$. We are going to compare the presented algorithm with this simple method, which we will refer to as the *brute-force* algorithm. In this example, we

transform the RV ϕ for the initial velocity into a new random variable for the final position at t but the map g describing the transformation is no longer monotone, as one can see from the elementary examples, taken from physical and mechanical models, shown below (see Figure 3.2 and Figure 3.3 for two possible cases).

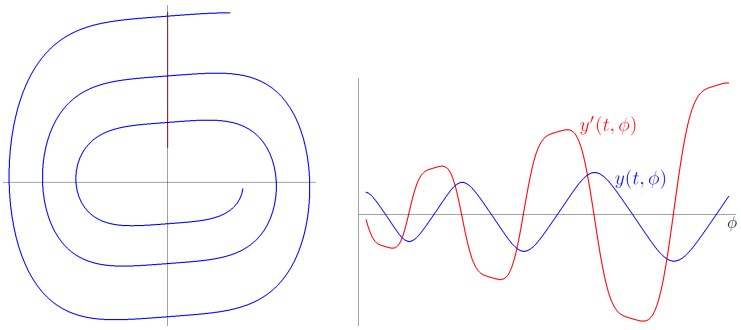

Figure 3.2: The figure illustrates the use of the shooting method for the Duffing equation, Eq. (3.6).

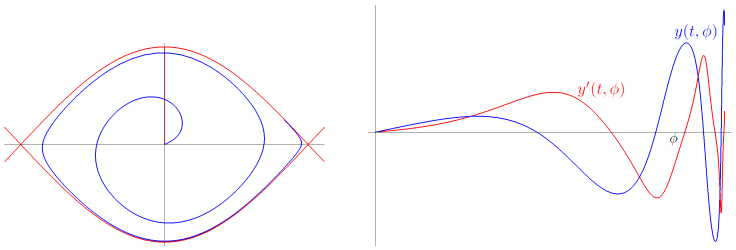

Figure 3.3: The figure illustrates the use of the shooting method for the pendulum equation, Eq. (3.7).

In Figure 3.2, we consider the Duffing equation

$$y''(t) + \rho(y(t)) = 0, \tag{3.6}$$

with the superlinear term $\rho(y) = 4y^3$. In this case, it is well-known that the origin is a global center in the phase plane $(y, v) = (y, y')$ and all the orbits around the origin lie on the energy levels $\frac{1}{2}v^2 + y^4 = \text{constant} > 0$. The left panel shows the image of the Poincaré map after time $t = 10$ of the vertical segment $y(0) = 0$, $y'(0) = \phi \in [1, 5]$. The right panel shows the graph of the map φ which associates to $\phi \in [1, 5]$ the value of the solutions $y(t, \phi)$, respectively $y'(t, \phi)$, at the time $t = 10$.

In Figure 3.3, we represent the pendulum equation

$$y''(t) + \sin(y(t)) = 0, \tag{3.7}$$

where the origin is a local center in the phase plane $(y, v) = (y, y')$ bounded above and below by two heteroclinic trajectories. These heteroclinic trajectories connect the unstable equilibrium points $(\pm\pi, 0)$, which represent the geometric configuration of a pendulum going to the inverted vertical position. For an energy constant $0 < c < 2$, all the orbits around the origin lie within the energy levels $\frac{1}{2}v^2 + (1 - \cos(y)) = c$ and are closed curves relatively to the strip $]-\pi, \pi[\times\mathbb{R}$. The left panel shows the image of the Poincaré map after time $t = 20$ of the vertical segment $y(0) = 0$, $y'(0) = \phi \in]0, 1.998]$. The right panel shows the graph of the map φ which associates to $\phi \in [1, 5]$ the value of the solutions $y(t, \phi)$, respectively $y'(t, \phi)$, at the time $t = 20$.

Both numerical examples above provide simple cases from classical physical problems, in which the map g, is far from being monotone.

c) As a third example, we consider a variant of case b), where the dependence of the solution on a random parameter is more involved. We study a second-order problem of the form

$$\begin{cases} y''(t) + f\big(y(t), y'(t), t\big) = k\phi \\ y(t_0) = a(\phi),\ y'(t_0) = b. \end{cases} \tag{3.8}$$

where we have consider a more general dependence on the single random variable other than in the initial conditions, although the RV does not change with time. In this third instance, we can produce very complicated non-monotone maps from apparently rather simple boundary value problems. let us consider harmonic oscillator with constant external force,

$$\frac{1}{\omega^2} y''(t) + y(t) = k\phi \tag{3.9}$$

which produces the mapping

$$\varphi(\phi, t) = k\phi + A\cos(\omega t + \phi). \tag{3.10}$$

In addition, we further assume the following initial conditions

$$y(0) = k\phi + A, \quad y'(0) = 0.$$

This example will be analyzed more in detail in the next section.

Therefore, as we mentioned above, the aim of the present paper is to introduce a new method for the numerical approximation of μ_Y from a given μ_X in cases

in which the theoretical procedure described the formula (3.1) is not effectively applicable. Moreover, we stress that our method can be applied even if we do not have an analytical expression of the function g, which however can be numerically constructed. This is particularly relevant because, in most of the physical applications, the transformation is obtained only in the last way.

Our approach is developed in detail in Section 3.2. In Section 3.3 we apply our theory to the example given by (3.10), as a proof of concept. The implemented algorithm is presented in Section 3.4. Finally, in Section 3.5 we provide some further numerical examples where we compare our new method, with the application of (3.1) and with the brute force approach. From these examples, the advantage of the new point of view will be evident particularly with respect to the numerical applications.

3.2 The problem and a fast introduction to FDF

Let us consider an ordinary differential system (like, for instance, (3.5)) where the initial conditions depend on a one-dimensional unknown random number ϕ with mass probability function $\mu : [\alpha, \beta] \subset \mathbb{R} \to \mathbb{R}$. As a typical application we might consider a projection of the solution onto a one-dimensional subspace, thus obtaining a new mass probability distribution function (PDF) $\psi(y, t)$ that evolves in time. That is, we look for the PDF $\mu_Y := \psi(y, t)$ that describes the probability of finding our system in the position y at time t, provided that we know the probability distribution $\mu_X := \mu(\phi)$.

For each $\phi \in [\alpha, \beta]$, the (projected) deterministic solution of the differential equation is a function $\varphi_\phi(t) : [0, t_{max}] \to \mathbb{R}$ that describes how the system evolves in time t. Under standard smoothness conditions on the vector field (cf. [13]) the function $\varphi(\phi, t) := \varphi_\phi(t)$ is of class $\mathcal{C}^1\big([\alpha, \beta] \times [0, t_{max}]\big)$. As we have discussed in the introduction, for any fixed $t > 0$, the map $\phi \mapsto \varphi_\phi(t)$ may be non-invertible. The idea behind the present work is that the evolution in space $y(t) = \varphi(\phi, t)$ of the system, spreads, squeezes or stretches and overlaps or folds the probability mass $\mu(\phi)$ in the space. Then we propose to replace the representation of the physical system given by $\varphi(\phi, t)$, with a new mathematical entity, which we call *folding domain function FDF*, such that we can determine $\psi(y, t)$ with the minimum computational cost. Although in the present demonstration the FDF method is applied assuming that we already know the analytical solution φ of the mapping, this does not affect the applicability of the FDF algorithm (FDF-A) to cases where the differential system is not analytically solvable, but a suitable approximation to the solution can be obtained from *numerical integrators*. As a matter of fact, the FDF-A algorithm only requires the knowledge of a finite set of values $\varphi_i := \varphi(\phi_i, t)$

(with $i \in \{1, \dots, N_{div}\}$ and $N_{div} \in \mathbb{N}$), for some initial conditions $\phi_i \in [\alpha, \beta]$, which contain all the relevant information for the mapping and that we will define later on. Interestingly, these particular values can be determined from the knowledge of the analytical solution of the differential equation but, more important, from the application of any numerical solver of the initial value problem.

3.2.1 The folding domain functions

Let X be a RV defined on a probabilistic measure space with values in a compact interval $[\alpha, \beta]$ and let $g : [\alpha, \beta] \to [g_{\min}, g_{\max}]$ be a continuously differentiable function which is strictly piecewise monotone. Accordingly, we decompose the domain of g into a finite sequence of adjacent intervals, by setting

$$\alpha = \alpha_0 < \alpha_1 < \cdots < \alpha_{j-1} < \alpha_j < \dots \alpha_k = \beta,$$

with the convention that g is strictly monotone with nonzero derivative on each subinterval $]\alpha_{j-1}, \alpha_j[$ and, moreover, each α_j with $0 < j < k$ is a stationary point which is a strict local maximum or local minimum. Let also

$$A := \{\alpha_j : j = 0, \dots, k\}.$$

Notice that, by construction, the map g is strictly increasing/decreasing restricted between two consecutive points in A. It will be also convenient to introduce the following notation

$$\begin{cases} A_j := [\alpha_{j-1}, \alpha_j[, \quad \text{for } \ j = 1, \dots, k-1 \\ A_k := [\alpha_{k-1}, \alpha_k] = [\alpha_{k-1}, \beta], \end{cases}$$

so that the intervals A_j $(j = 1, \dots, k)$ determine a partition of the interval $[\alpha, \beta]$.

We define the vector $\Lambda := (\lambda_1, \dots, \lambda_k)$, where, for each $j = 1, \dots, k$, we set

$$\lambda_j := g(\alpha_j) - g(\alpha_{j-1})$$

(see Figure 3.4 for an illustrative example). We also introduce the constant

$$S = S_\Lambda := \sum_{j=1}^{k} |\lambda_j|.$$

As a next step, we define the transformation $\hat{g} : [\alpha, \beta] \to [0, S]$ as

$$\begin{cases} \hat{g}(x) = m_{j-1} + |g(x) - g(\alpha_{j-1})|, \quad \text{for } \ x \in [\alpha_{j-1}, \alpha_j] \\ j = 1, \dots, k, \end{cases} \tag{3.1}$$

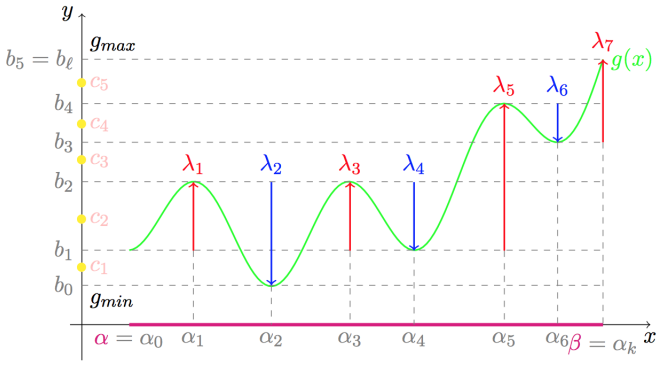

Figure 3.4: The function g.

where

$$m_0 = 0 \quad \text{and} \quad m_j := |\lambda_1| + \cdots + |\lambda_j|, \quad j = 1, \ldots, k.$$

By definition, $\hat{g}(\alpha) = 0$ and $\hat{g}(\beta) = S$. The formula (3.1) defining $\hat{g}$ is introduced as a way to unfold the graph of g. Indeed, transformation $\hat{g}$ acts as follows: given a graph of a piecewise monotone function g, first we shift it as to have value 0 at $x = \alpha$. Then, if $[\alpha_{j-1}, \alpha_j]$ is an interval where g is increasing, we further shift this portion of the graph of g by the quantity $m_{j-1} - g(\alpha_{j-1}) = |\lambda_1| + \cdots + |\lambda_{j-1}| - g(\alpha_{j-1})$. On the other hand, if $[\alpha_{j-1}, \alpha_j]$ is an interval where g is decreasing, we reflect the graph of g symmetrically with respect to the horizontal line $y = g(\alpha_{j-1})$ and then we shift it as to obtain the graph of a continuous and monotonously increasing function (see Figure 3.5 for an illustrative example). Observe that, if g is smooth (of class C^1), $\hat{g}$ is smooth, too.

By construction, for any continuously differentiable and piecewise monotone function $g : [\alpha, \beta] \to [g_{\min}, g_{\max}]$ we have that $\hat{g} : [\alpha, \beta] \to [0, S]$ is strictly monotonously increasing with inflection points at α_i $(i = 1, \ldots, k-1)$ and, moreover,

$$\frac{d}{dx}\hat{g}(x) = \left| \frac{d}{dx} g(x) \right|, \quad \forall\, x \in [\alpha, \beta].$$

At this point, the inverse function of $\hat{g}$ is well defined as

$$\eta : [0, S] \to [\alpha, \beta].$$

This new map is again strictly monotonously increasing and continuously differentiable on $[0, S] \setminus \{\hat{g}(\alpha_i), i = 1, \ldots, k-1\}$, where the derivative in the excluded points exists with value $+\infty$ (see Figure 3.6).

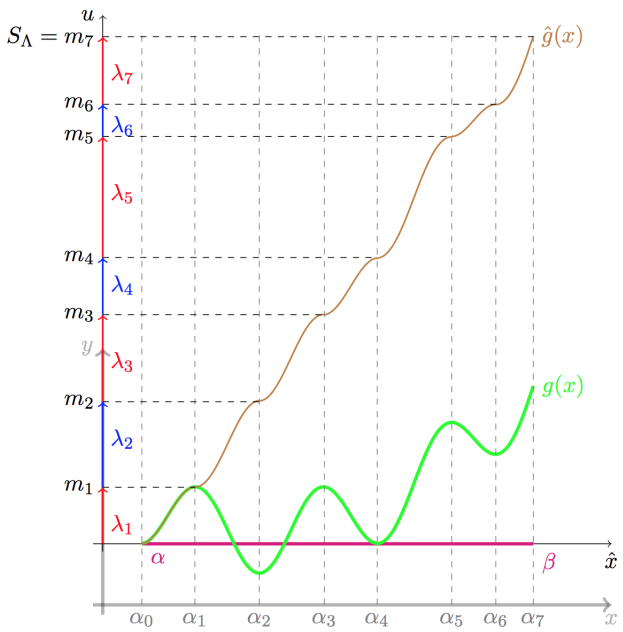

Figure 3.5: The functions g and $\hat{g}$.

Let us consider the set

$$B = \{g(\alpha_i), i = 0, \dots, k\} = \{b_0, b_1, \dots, b_\ell\},$$
$$\text{with} \qquad g_{\min} = b_0 < b_1 < \cdots < b_\ell = g_{\max}$$

and decompose $[g_{\min}, g_{\max}]$ into non-overlapping sets B_i as

$$[g_{\min}, g_{\max}] = B_1 \cup B_2 \cup \cdots \cup B_\ell,$$

where

$$\begin{cases} B_i := [b_{i-1}, b_i[, & \text{for } \ i = 1, \dots, \ell - 1 \\ B_\ell := [b_{\ell-1}, b_\ell] = [b_{\ell-1}, g_{\max}]. \end{cases}$$

Note that for each $y \in [g_{\min}, g_{\max}]$ there is a (nonempty) finite set of points in the inverse image $g^{-1}(\{y\}) \subset [\alpha, \beta]$. Thus the (finite) set of indexes

$$I(y) := \{j \in \{1, \dots, k\} : \exists\, x \in A_j \ : g(x) = y\}$$

is well defined.

Lemma 1. *If $W \subset [\alpha, \beta]$ is an open interval such that $g(W) =]b_{i-1}, b_i[$ for some $i \in \{1, \dots, \ell\}$, then g is strictly monotone in W.*

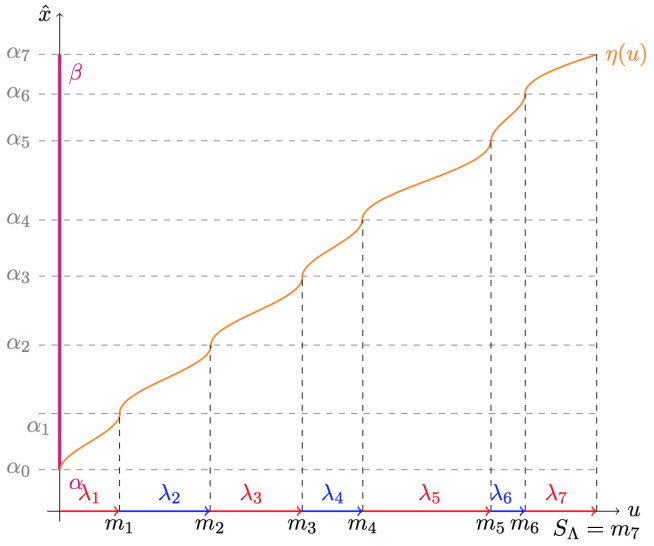

Figure 3.6: The function η.

Proof. For the proof it is sufficient to observe that, by our assumption, the only possible critical points of g are contained in the set A. On the other hand, $B = g(A)$ and $]b_{i-1}, b_i[\subset [g_{\min}, g_{\max}] \setminus B$. As a consequence, $g'(x) \neq 0$ for all $x \in W$ and therefore, g is strictly monotone in W. □

Lemma 2. *For each $y \in]b_{i-1}, b_i[$ (where $i \in \{1, \ldots, \ell\}$ an arbitrary index), the set $I(y)$ is constant. Therefore, $I(y) = I(c_i)$ where $c_i := \frac{b_{i-1}+b_i}{2}$.*

Proof. For a fixed $i \in \{1, \ldots, \ell\}$, let us consider the middle point $c_i := \frac{b_{i-1}+b_i}{2}$ and let $\gamma_1 < \gamma_2 < \cdots < \gamma_p$ be such that $g^{-1}(\{c_i\}) = \{\gamma_1, \ldots, \gamma_p\}$. For each γ_s, with $s = 1, \ldots, p$, let W_s be an open maximal interval containing γ_s and such that $g(W_s) =]b_{i-1}, b_i[$. By Lemma 1, g is strictly monotone on W_s and, therefore, the open intervals W_s are pairwise disjoint. In fact, if, by contradiction, two of these intervals, say W_s and W_r, overlap, then $W_s \cup W_r$ turns out to be a unique interval W such that $g(W) =]b_{i-1}, b_i[$ and hence g must be strictly monotone on W, contradicting the fact that $g(\gamma_s) = g(\gamma_r) = c_i$ (with $\gamma_s \neq \gamma_r$). As a consequence of the fact that the open intervals are pairwise disjoint, we conclude that

$$g^{-1}(\,]b_{i-1}, b_i[\,) = W_1 \cup \ldots W_p$$

and then

$$\#g^{-1}(\{y\}) = \text{constant}, \quad \forall\, y \in]b_{i-1}, b_i[,$$

where $\#E$ denotes the cardinality of the set E (in our case it is just the number of points, as all the involved sets are finite).
As a final observation, we claim that each of the intervals W_s is contained in exactly one of the intervals A_j. Indeed, let $r \in \{1, \dots, p\}$ be such that $W_r \subset]\alpha_{j-1}, \alpha_j[$ and let $s \neq r$. If, by contradiction, also $W_s \subset]\alpha_{j-1}, \alpha_j[$, then $\gamma_r, \gamma_s \in]\alpha_{j-1}, \alpha_j[$ with $\gamma_r \neq \gamma_s$ and $g(\gamma_r) = g(\gamma_s) = c_i$, contrary to the fact that g is strictly monotone on $A_j = [\alpha_{j-1}, \alpha_j]$.

This latter observation guarantees that $I(y)$ is constant for each $y \in]b_{i-1}, b_i[$ and the proof is complete. □

Remark 1. *It is interesting to observe that the result about the constancy of* $\#g^{-1}(\{y\})$ *for all* $y \in]b_{i-1}, b_i[$ *is a general property which is valid also for locally invertible and proper maps on metric spaces, as proved in [14, §3].*

As a next step we want to introduce a formal method to determine, for a given $y \in [g_{\min}, g_{\max}]$, the set $I(y)$. We will treat separately the case when $y = b_i$, or $y \in]b_{i-1}, b_i[$ (for some $i \in \{1, \dots, \ell\}$). The first situation concerns the analysis of a finite set and will be treated in a second moment. Concerning the second case, by virtue of Lemma 2, it will be sufficient to consider $I(c_i)$, where c_i is the middle point of each interval. It is straightforward to check that $y \in]g(\alpha_{j-1}), g(\alpha_j)[$ (when $g(\alpha_{j-1}) < g(\alpha_j)$) or, respectively $y \in]g(\alpha_j), g(\alpha_{j-1})[$ (when $g(\alpha_{j-1}) > g(\alpha_j)$), provided that

$$0 < (y - g(\alpha_{j-1}))\text{sign}(\lambda_j) < |\lambda_j|, \tag{3.2}$$

a condition which can be easily implemented from an algorithmic point of view. To better understand the meaning of (3.2), recall that $\text{sign}(\lambda_j)$ determines whether g is increasing or decreasing on each interval $[\alpha_j, \alpha_{j+1}]$.

Since the map g is (in general) non-invertible, the idea now is to spread the point y on the interval $[0, S]$, which is the range of the function $\hat{g}$ and the domain of the function η, in such a way that, at each $y \in]b_{i-1}, b_i[$, we associate a set of points

$$u_{\rho_1}(y), u_{\rho_2}(y), \dots, u_{\rho_p}(y), \quad \text{for } I(y) = \{\rho_1, \rho_2, \dots, \rho_p\}.$$

More precisely, we obtain these values by setting

$$u_j(y) = m_{j-1} + (y - g(\alpha_{j-1}))\text{sign}(\lambda_j), \quad \text{for } j \in I(y). \tag{3.3}$$

Then, by means of the inverse mapping η, we can obtain the set of points of the initial domain which share the same image y. More formally, we have that

$$x_j(y) = \eta(u_j(y)) = \left(g|_{]\alpha_{j-1}, \alpha_j[}\right)^{-1}(y), \quad \text{for } j \in I(y).$$

which is the collection of points in the domain of g that share the same image. In conclusion, via the function η we obtain a cumulative inverse of all the local inverse functions of g restricted to the single intervals A_j, where g is strictly monotone.

We summarise the procedure described above, by recalling the previous diagrams. We start in Figure 3.4 from a function g where we split its domain into a finite number of adjacent intervals where g is either strictly increasing or strictly decreasing. On the vertical axis we have also indicated the set of points $B = \{b_0, \ldots, b_\ell\}$ which is the set $\{g(\alpha_0), \ldots, g(\alpha_k)\}$ with its elements arranged in the natural order. The figure also provides a visual illustration of Lemma 2. Indeed, it is apparent that $I(y)$ is constant and equal to $I(c_i)$ for each $y \in]b_{i-1}, b_i[$. The same figure also puts in evidence the vector $\Lambda = (\lambda_1, \ldots, \lambda_k)$.

Figure 3.5 illustrates the transformation $g \mapsto \hat{g}$ and reports the starting coordinate system (x, y) and the translate $(\hat{x}, u)$, which shifts $g(\alpha_0)$ to 0. The figure also puts in evidence the new special points m_i on the u-axis.

Finally, Figure 3.6 shows the graph of the function $\eta = \hat{g}^{-1}$. As explained theoretically above, for any given image y we have a method to "invert" the function g via the function η, provided that we correctly associate the set of points $u_j(y)$ for $y \in I(y)$ to $y \in [g_{\min}, g_{\max}]$

It remains to discuss the case when $y \in B$, namely when $y = b_i$ for some $i = 0, \ldots, \ell$. We recall that for these points, it may exist $x_j(y)$ such that $g'(x_j(y)) = 0$. The fact that the $\#B$ is finite assures that these points are irrelevant in probability theory as they represent a ensemble of zero measure. However, we provide a more detailed demonstration for completeness.

We start by mentioning again that $\#g^{-1}(\{y\})$ is constant only on $]b_i, b_{i+1}[$ (according to Lemma 2), but it changes at the ends of the interval. In general, the set $g^{-1}(\{b_i\})$ contains at least a critical point α_j (with $j = 1, \ldots, k-1$) or an extreme point α_j (with $j = 0, k$) and, possibly other points in the interior of the intervals A_j where g is strictly monotone. This situation is evident from the example in Figure 3.4: the $g^{-1}(\{b_3\})$ contains a regular point and a critical point of minimum; When we increase y passing across b_3, we find $1-2-3$ solutions. On the other hand, the set $g^{-1}(\{b_4\})$ contains a regular point and a critical point of maximum and then, when we increase y passing across b_4, we find $3-2-1$ solutions. This example reflects a general situation and suggests the need to distinguish, among the critical points,the strict local minima and the strict local maxima. This intuitive explanation is now formalised in what follows.

We split $g^{-1}(\{b_i\})$ as

$$g^{-1}(\{b_i\}) = \mathfrak{C}_m^i \cup \mathfrak{C}_M^i \cup \mathfrak{R}^i \cup \mathfrak{E}_m^i \cup \mathfrak{E}_M^i,$$

where $\mathfrak{C}_m^i$ and $\mathfrak{C}_M^i$ denote the sets of critical points which are interior strict local minima or strict local maxima, respectively, while $\mathfrak{R}^i$ is the set of regular points

in the interior of the interval. We denote by $\mathfrak{E}_m^i$ and $\mathfrak{E}_M^i$ the sets of extreme points $\{\alpha, \beta\}$ (having b_i as image) which are, respectively, local minima or local maxima. Now the rule to count the number of inverse images passing from an interval $]b_{i-1}, b_i[$ to the next one $]b_i, b_{i+1}[$ across the point b_i is given by:

$$\#I(c_{i+1}) = \#I(c_i) + 2\#\mathfrak{C}_m^i - 2\#\mathfrak{C}_M^i - \#\mathfrak{E}_M^i.$$

Respectively, the rule passing from an interval $]b_i, b_{i+1}[$ to the previous one $]b_{i-1}, b_i[$ across the point b_i is given by:

$$\#I(c_i) = \#I(c_{i+1}) - 2\#\mathfrak{C}_m^i + 2\#\mathfrak{C}_M^i - \#\mathfrak{E}_m^i.$$

Conversely, if we know the type of the points in $g^{-1}(\{b_i\})$, we can determine the number of elements of $I(y)$ for y in an interval having b_i as an extremal point. In fact, the following holds:

$$\#I(y) = \#g^{-1}(\{b_i\}) + \#\mathfrak{C}_m^i - \#\mathfrak{C}_M^i - \#\mathfrak{E}_M^i, \quad \forall\, y \in]b_i, b_{i+1}[\,.$$

To justify the above formula, we observe that if $b_i = g(\alpha_j)$ (for some $j = 1, \ldots, k-1$), where α_j is an interior point of strict local minimum, then for $\varepsilon > 0$ and sufficiently small we have exactly two points $x_{j,\text{left}} < \alpha_j < x_{j,\text{right}}$ in a (small) neighborhood of α_j such that $g(x_{j,\text{left}}) = g(x_{j,\text{right}}) = y$. If $b_i = g(\alpha_j)$ (for $j = 0, k$) is the image of an extreme point which is a local minimum, then there is exactly one point $\tilde{x}$ in a right neighborhood of α (respectively in a left neighborhood of β) such that $g(\tilde{x}) = y$. If $b_i = g(x^*)$ for some $x^* \in \mathfrak{R}^i$, we have that g is strictly monotone (increasing or decreasing) in an open interval containing x^* and therefore there exists a unique point in such an open interval having y as image. Finally, if $b_i = g(\alpha_j)$ for some $j = 0, \ldots, k$ with α_j a point of local maximum (in the interior or at the boundary of $[\alpha, \beta]$), there are no solutions of $g(x) = y$ in a neighborhood of α_j. In this manner we have counted all the possible solutions of $g(x) = y \in]b_i, b_i + \varepsilon[$ for $\varepsilon > 0$ and sufficiently small. Taking into account that the number of these solutions is constant in the open interval $]b_i, b_{i+1}[$ we have proved the above formula.

In a similar manner we prove that

$$\#I(y) = \#g^{-1}(\{b_i\}) - \#\mathfrak{C}_m^i + \#\mathfrak{C}_M^i - \#\mathfrak{E}_m^i, \quad \forall\, y \in]b_{i-1}, b_i[\,.$$

As a final step, we propose a visual description (see Figure 3.7) to detect the inverse images of a point $y \in [g_{\min}, g_{\max}]$ using the components of the vector Λ and the set $I(y)$.

Our procedure consists in starting from the point $g(\alpha_0) = b_{i^*} \in B$ (for some $i^*\{1, \ldots, \ell\}$) and superimpose suitable *layers* by taking $\lambda_1, \ldots, \lambda_k$. All the points b_i are obtained as points of the form

$$b_{i^*} + \lambda_1 = g(\alpha_1), \quad b_{i^*} + \lambda_1 + \lambda_2 = g(\alpha_2), \ \ldots, \ b_{i^*} + \sum_{j=1}^{k} \lambda_j = g(\alpha_k) = g(\beta).$$

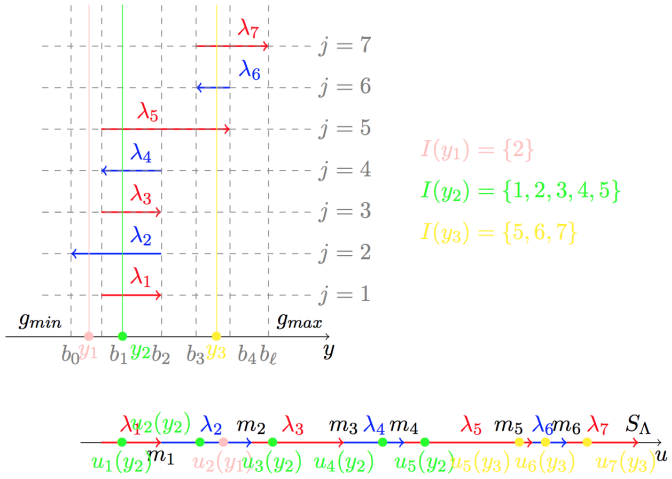

Figure 3.7: The layers.

Once the points $g(\alpha_j)$ are arranged in the natural order for the set B, as $\{b_1, \ldots, b_\ell\}$, for any fixed $\bar{y} \in]b_{i-1}, b_i[$, in order to determine the set $I(y)$, we have just to look for the number of layers meeting the vertical line $y = \bar{y}$ (as observed above in Lemma 2, we can take $\bar{y} = c_i$). The corresponding scheme is illustrated in Figure 3.7 below. For the figure we take as a function g, the one reported in Figure 3.4.

Remark 2. *In the sequel we will apply the method described above to maps obtained from a class of random dynamical systems. In this case, the function g comes from a map $\varphi(x, t)$, for a fixed value of the time t. The derivative of the auxiliary function η will determine the density of a composite RV. From a topological point of view, the evolution of $\varphi(x, t)$, as t varies in a time-interval, can be interpreted as sequence od functions $g_t(x)$ which transform (fold) the RV X (with values in $[\alpha, \beta]$) and mass probability function μ_X into a new RV $Y_t = g_t(X)$. In this perspective, it is natural to consider the above method as a technique which at any time t "unfolds"*

the range $[g_{\min}, g_{\max}]$ *of* g *to the new range* $[0, S_\lambda]$ *which becomes the new domain of the function* η*, as shown in the example of Figure 3.7.*

3.2.2 The connection with the theory of Random Variable Transformation

Let X be a RV with range in a compact interval $[\alpha, \beta]$ and let $g : [\alpha, \beta] \to [g_{\min}, g_{\max}]$ be a smooth and piecewise monotone function as it is the one constructed in Section 3.2.1. Our goal is to show that the FDF is consistent with the general theory which provides the probability distribution function of the new RV $Y = g(X)$.

Using the same notation as in the previous section, given any $\tilde{y} \in]b_{i-1}, b_i[$ and a sufficiently small $\varepsilon > 0$ such that

$$]\tilde{y} - \varepsilon, \tilde{y} + \varepsilon[\subset]b_{i-1}, b_i[,$$

according to Lemma 2 we have that the set of indices $I(y)$, representing the layers associated with y, is constant for all $y \in]\tilde{y} - \varepsilon, \tilde{y} + \varepsilon[$. Thus,

$$\begin{aligned}
P(\tilde{y} - \varepsilon < Y < \tilde{y} + \varepsilon) &= P\big(X \in g^{-1}(\,]\tilde{y} - \varepsilon, \tilde{y} + \varepsilon[\,)\big) \\
&= \sum_{j \in I(\tilde{y})} P\big(X \in (g|_{A_j})^{-1}(\,]\tilde{y} - \varepsilon, \tilde{y} + \varepsilon[\,)\big) \\
&= \sum_{j \in I(\tilde{y})} P\big(X \in \eta\big(\,]u_{j,\min}(\tilde{y}), u_{j,\max(\tilde{y})}[\,\big)\big) \\
&\quad u_{j,\min}(\tilde{y}) := \min\{u_j(\tilde{y} - \varepsilon), u_j(\tilde{y} + \varepsilon)\}, \\
&\quad u_{j,\max}(\tilde{y}) := \max\{u_j(\tilde{y} - \varepsilon), u_j(\tilde{y} + \varepsilon)\} \\
&= \sum_{j \in I(\tilde{y})} \int_{\min\{u_j(\tilde{y}-\varepsilon), u_j(\tilde{y}+\varepsilon)\}}^{\max\{u_j(\tilde{y}-\varepsilon), u_j(\tilde{y}+\varepsilon)\}} \mu_X(\eta(u))\eta'(u)du \\
(*) &= \sum_{j \in I(\tilde{y})} \int_{\tilde{y}-\varepsilon}^{\tilde{y}+\varepsilon} \mu_X(\eta(u(\xi)))\eta'(u(\xi)) \left|\frac{du(\xi)}{d\xi}\right| d\xi \\
(*) &= \sum_{j \in I(\tilde{y})} \int_{\tilde{y}-\varepsilon}^{\tilde{y}+\varepsilon} \mu_X((g|_{A_j})^{-1}(\xi)) \left|\frac{d}{d\xi}(g|_{A_j})^{-1}(\xi))\right| d\xi.
\end{aligned}$$

where, in this equation g^{-1} does not strictly stand for the inverse of g, which generally speaking is not invertible, but it represents the collection of pre-images of the segment $]\tilde{y}-\varepsilon, \tilde{y}+\varepsilon[$. In contrast, $(g|_{A_j})^{-1}$ represents the actual local inverse

of the segment for the set A_j. Moreover, in the last two steps (indicated by $(*)$), we have used the fact that

$$\eta'(u(y))\left|\frac{du(y)}{dy}\right| = \left|\frac{d}{dy}(g|_{A_j})^{-1}(y)\right|$$

and also that in fact, $\frac{du(y)}{dy} = \pm 1$.

On the other hand, by definition,

$$P(\tilde{y}-\varepsilon < Y \leq \tilde{y}+\varepsilon) = \int_{\tilde{y}-\varepsilon}^{\tilde{y}+\varepsilon} \mu_Y(\xi)d\xi.$$

Therefore, comparing the two expressions, we obtain that

$$\mu_Y(y) = \sum_{j\in I(y)} \mu_X((g|_{A_j})^{-1}(y))\left|\frac{d}{dy}(g|_{A_j})^{-1}(y))\right|, \tag{3.4}$$

holds for all $y \in [g_{\min}, g_{\max}] \setminus B$. In this manner, we have reestablished (3.1), for $h_i := (g|_{A_j})^{-1}$ indicating that the FDF method is consistent with the general theory for the RVT. Eq. (3.4) also holds for the segment end points $y = g(\alpha_0) = g(\alpha)$ (respectively, for $y = g(\alpha_k) = g(\beta)$) provided that they are not a *critical value*. The formula is not applicable to the critical values $b_0, \ldots, b_\ell$ because for these points the derivative of the inverse function is infinite. Notice that such a limitation is also present in the general RVT theory as expressed in (3.1). However, in our situation, as the number of critical values is finite the ensemble of critical points of g in the interval $[\alpha, \beta]$ is thus a set of zero measure. Therefore, the weight of the critical values is negligible in the computation of the cumulative distribution function F_Y, provided that X is a continuous RV or a discrete/mixed one with a finite number of jumps at points which are not critical. Finally, in the very special case in which there are jumps for the RV X at some critical points of g, the problem will be solved by a direct computation as a limit from the neighboring compact environment.

3.3 An example

In order to demonstrate the applicability of the method, we start with a concrete example. Let us assume that our RDE admits an analytical solution $y(t) := \varphi(\phi, t)$. For example, recalling that the RDE Eq. (3.9) leads to solutions of the form (3.10), we assume that our physical system evolves according to:

$$\varphi(\phi, t) := k \cdot \phi + A \cdot \cos(\omega t + \phi), \tag{3.1}$$

Where $k > 0$ is a given constant, $A > 0$ is the *amplitude*, $\omega > 0$ is the *angular frequency*, and ϕ is the *initial phase*. Furthermore we assume that $\phi = X$ is a random number that belongs to the interval $[\alpha, \beta]$. We suppose that ϕ has mass probability function:

$$\mu_X : [\alpha, \beta] \subset \mathbb{R} \to \mathbb{R}. \tag{3.2}$$

In each fixed time instant $t = t^* > 0$ the physical system is in the position $y(t^*) = \varphi(\phi, t^*)$ and such a position depends on the particular initial phase $\phi \in [\alpha, \beta]$. We notice that, from the mathematical point of view, $y = \varphi(\phi, t)$ is a scalar field $\varphi : [\alpha, \beta] \times [0, t_{max}] \subset \mathbb{R}^2 \to \mathbb{R}$ that associates to each element (ϕ, t) a point y in the real physical space. Our idea is that, in each instant of time $t^* \in [0, t_{max}]$, we can get the probability mass function $\mu_Y := \psi(y, t^*)$ for the variable $y(t^*)$ by applying the new formal concept introduced above. We start by replacing the physical map given by Eq. (3.1) by the FDF, motivated by the theoretical results of the previous section. In Figure 3.8 we report the plot of the functions (3.1), corresponding to the physical solution in the (ϕ, t) plane (yelow), together with (3.2), giving the probability distribution of the random variable X. On the right-hand side of the figure we have singled out three instants of time $0 < t_1^* < t_2^* < t_3^* < t_{max}$, to show that the problem depends on the final time chosen for the analysis. In each of these times, we plot a function $g_{t_i^*} : [\alpha, \beta] \subset \mathbb{R} \to \mathbb{R}$ ($i \in \{1, 2, 3\}$), such that:

$$\begin{aligned} g_{t_1^*}(\phi) :=& \varphi(\phi, t_1^*), \\ g_{t_2^*}(\phi) :=& \varphi(\phi, t_2^*), \\ g_{t_3^*}(\phi) :=& \varphi(\phi, t_3^*). \end{aligned}$$

We notice that each of these three functions maps the interval $[\alpha, \beta]$ on the $x = \phi$-axis in a non-bijective way to the y-axis. As explained, we proceed to the separation of $g_{t_i^*}(\phi)$ into all the monotone pieces as we vary ϕ from α to β, as we described. Second, we identify the increasing from the decreasing pieces to construct $\hat{g}_{t_i^*}(\phi)$. As each of these pieces are invertible, we can calculate the transformation of μ_X into the *unfolded intermediate* $\tilde{\mu}_Y^t$, with $t = t_1^*, t_2^*, t_3^*$. Then, following the indicated procedure, we construct the final folded μ_Y. The key element is to realising that the *folding* process will introduce the overlap of the different sections. In Figure 3.8 we show precisely the overlapping pieces that will give rise to the final μ_Y.

In more detail, for each $t = t_1^*, t_2^*, t_3^*$ we have a different vector $\Lambda = \Lambda_t$ which collects all the needed set of information to construct the functions $\hat{g}$, η and the associated layers. For $t = t_1^*$, in Figure 3.8 the first arrow is a blue arrow that corresponds to the first decreasing part of $g_{t_1^*}$. The second is a red arrow that corresponds the increasing part of $g_{t_1^*}$ and the last one is another blue arrow that corresponds to the also decreasing part of $g_{t_1^*}$. We proceeded similarly for $g_{t_2^*}$ and

$g_{t_3^*}$. Observe that, as the time varies, the corresponding Λ_t changes and, therefore, the size and direction of the *arrows*, as well.

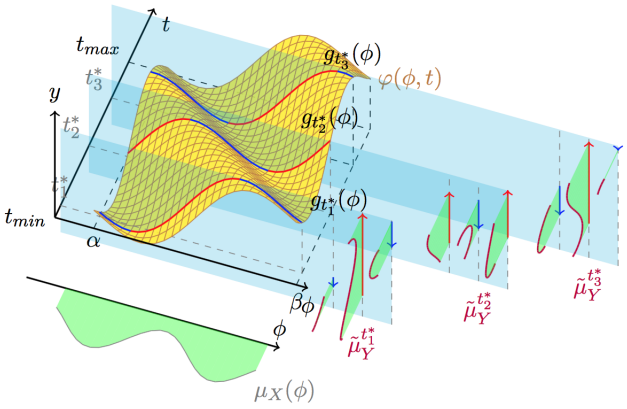

Figure 3.8: The physical system $\varphi(\phi,t) = k\cdot\varphi + A\cos(\omega t+\phi)$ and the *folding-domain function* approach.

Following Section 3.2.1, the procedure starts by replacing the description of the physical system given by $\varphi(\phi,t)$, for each $t\in[0,t_{max}]$, with:

1. the point $\chi_0(t) := \varphi(\alpha,t)$, corresponding to $g(\alpha_0) = g(\alpha) = g_t(\alpha)$,
2. the vector Λ_t that contains the arrows,
3. the function η_t,
4. according to (3.3), the functions $u_{i,t}(y)$, (with $i\in\{\rho_1,\dots,\rho_{p_t}(y)\} = I_t(y)$), which associate all the values $u_{\rho_1},\dots,u_{\rho_{p_t}}$ to each point y in the physical space, such that $\eta_t(u_i)=\phi_i$ and $\varphi(\phi_i,t)=y$.

We further notice that the bijection $\eta_{t_i^*}$ allows us to associate a probability weight $\tilde{\mu}_Y$ to each point on the three arrows via the PDF μ_X: indeed, in Figure 3.8, at the right-hand side, we show the graphs of three groups (for $t=t_1^*,t_2^*,t_3^*$) of three functions (over three arrows). We recall that we have denoted these three groups of functions (the so-called unfolded intermediate) as $\tilde{\mu}_Y^t$, with $t=t_1^*,t_2^*,t_3^*$. These three plots have been produced as a composition of μ_X with the inversions of $g_{t_i^*}$ in each of the three intervals of monotonicity in which the domain of μ_X is split. This can be obtained by choosing a point $u\in[0,S_{\Lambda_{t_i^*}}]$ and then by computing $\mu_X\left[\eta_{t_i^*}(u)\right]$. We stress that these composite graphs are represented just for the sake

of intuitively describing the underlying idea. The real graphs of μ_Y should take into account a scaling factor given by the inverse derivative and should be overlapped by the unfolding, summing up the different layers, according to (3.4).

The graphs of functions η_t are plotted in Figure 3.9. In both Figures 3.8 and 3.9 we consider three cases $t = t_1^*, t_2^*, t_3^*$ for which the same idea can be applied.

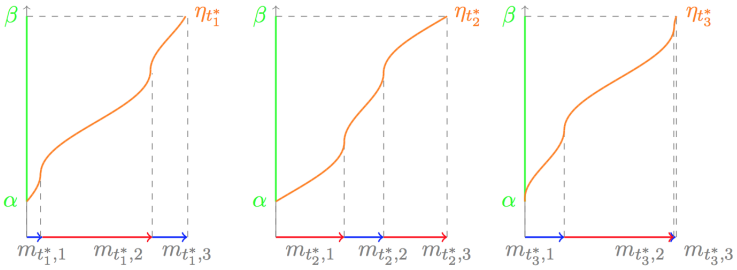

Figure 3.9: The functions $\eta_{t_1^*}$, $\eta_{t_2^*}$ and $\eta_{t_3^*}$ for different values of $t_1^* < t_2^* < t_3^*$.

Now we conclude this section providing an heuristic derivation of the PDF $\mu_Y = \psi(y,t)$. Let y be a point of the physical space where it exists a probability of finding the system, with respect to the random variable ϕ. The PDF $\psi(y,t)$ is obtained by determining all the points $\phi_i(y) \in [\alpha,\beta]$ such that $\varphi(\phi_i(y),t) = y$. Indeed, we expect that the probability of finding the system in y at time t can be obtained as the sum of the probabilities of all the values of $\phi_i(y)$ that will make the system to be in the position y at the time t. The subintervals within $[\alpha,\beta]$ where these $\phi_i(y)$ are located, are determined by the set of indexes $I_t(y)$. This is due to the fact that $\varphi(\phi,t)$ is *spreading* the mass probability μ_X around in the image space. In Figure 3.10 we show the regions where overlap will occur (darker green). In turn, in Figure 3.11 we show how this overlap will displace the resulting probability. For simplicity, however, in this later figure we have disregarded the Jacobian of the transformation in the summation of the different parts. However, this Jacobian is a essential part in the transformation as φ squeezes or stretches the probability mass $\mu(\phi)$ in the final space.This deformation also affects the final PDF ψ through the derivative (Jacobian) in (3.4). For example, when y corresponds to a local minimum or local maximum value of $\varphi(\phi,t)$, we expect a *peak of probability*. Indeed the derivative $\partial\varphi/\partial\phi$ is zero and then the derivative of the corresponding inverse auxiliary function η_t is infinity.

In summary, the main idea behind the FDF approach can be sketched in fol-

lowing scheme:

$$y \xrightarrow{u_{i,t}} \{u_{\rho_1}, \ldots, u_{\rho_{p_t}}\} \xrightarrow{\eta_t} \{\phi_i : i \in I_t(y)\} \xrightarrow{\mu_X} \ldots$$
$$\ldots \xrightarrow{\mu_X} \{\mu_X(\phi_i) : i \in I_t(y)\} \xrightarrow{\Sigma} \sum_{i \in I_t(y)} \mu_X(\phi_i(y)) \cdot \frac{d\eta_t}{du}(u_i), \tag{3.3}$$

where we recall that $\phi_i = \eta_t(u_i)$ for each $i \in I_t(y)$.

We want to emphasise that the FDF approach presents several advantages from the point of view of numerical implementation of an algorithm aiming at the RVT. In particular,

1. $u_{i,t}(x)$ is piecewise linear,

2. $\eta_t(u)$ is invertible,

3. both of these functions can be very easily determined numerically.

All these facts permits the use of an algorithm which is not based on the reconstruction of the final probability via the generation of bundles of trajectories, using the Monte Carlo method, and calculating the final probability through a histogram. Instead, the piece-wise nature of our approach allows us to construct the final solution through a more effective piece-wise analysis.

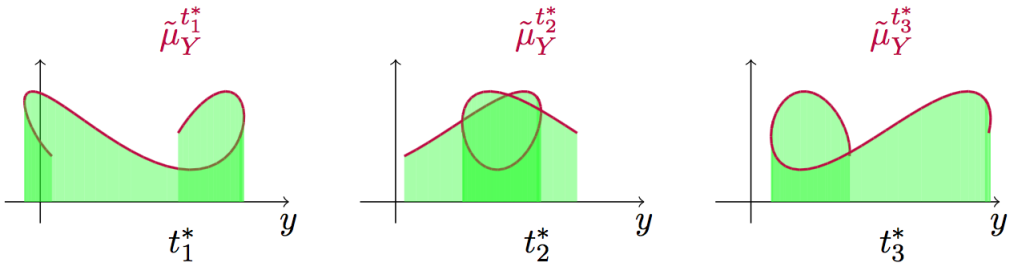

Figure 3.10: Here we have $t = t_1^*$, $t = t_2^*$ and $t = t_3^*$. We notice that $I_{t_1^*}(y) = \{1, 2\}$, $I_{t_1^*}(y) = \{2\}$ and $I_{t_1^*}(y) = \{2, 3\}$ as y varies from the $g_{t_1^*,\min}$ to $g_{t_1^*,\max}$. Similarly, the three cases of $t = t_2^*$ as y varies, are $I_{t_1^*}(y) = \{1\}$, $I_{t_1^*}(y) = \{1, 2, 3\}$ and $I_{t_1^*}(y) = \{3\}$. Finally, the three cases of $t = t_3^*$ as y varies, are $I_{t_1^*}(y) = \{1, 2\}$, $I_{t_1^*}(y) = \{2\}$ and $I_{t_1^*}(y) = \{2, 3\}$.

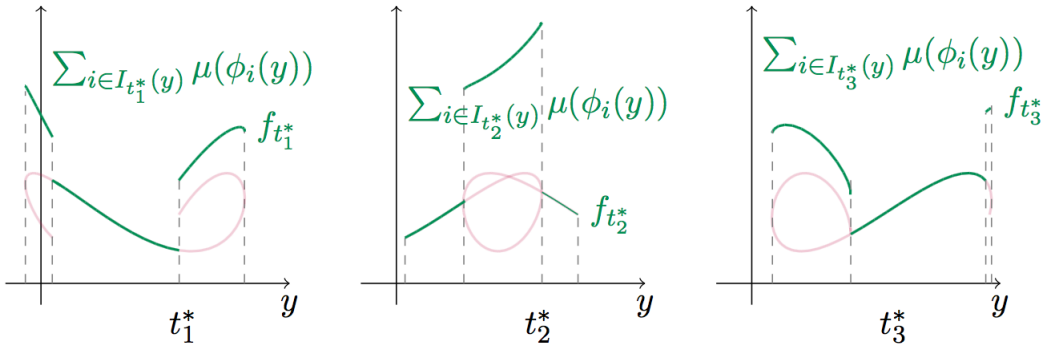

Figure 3.11: Functions $f_{t_1^*}$, $f_{t_2^*}$ and $f_{t_3^*}$. The graphs are obtained with $f_t = \sum_{i\in I_t(y)} \mu(\phi_i(y))$ for each $t \in \{t_1^*, t_2^*, t_3^*\}$. The function f_t represent the additive components in the last part of the formula (3.3) without the multiplicative factor $\frac{d\eta_t}{du}$.

3.4 The algorithm

In this section we present the application of the Folding Domain Function algorithm (FDF) to some cases of interest, in order to check its consistency by comparison with a brute force algorithm. As before, the dynamical system has a collection of solutions described by the function $\varphi(\phi, t)$, which parametrically depends on the random variable ϕ. In most of the cases of interest, such a solution can not be determined analytically and, therefore, approximations to the solution are generated *via* **Numerical integrators** [2].

3.4.1 The brute force algorithm

The algorithm based on the Monte Carlo generation of instances of the RV ϕ will be referred to as the *brute-force* algorithm. We use this method for comparison with the FDF results and is described in the following list the steps:

1. We numerically generate a large number of points $\phi \in [\alpha, \beta]$ distributed according to the known PDF $\mu : [\alpha, \beta] \to \mathbb{R}_{\geq 0}$. Typically, computers provide uniform as well as Gaussian random number generators, which could be used at this point to generate any general distribution function μ for the random number ϕ, provided that the latter is well behaved.

[2] In our examples we have used those already implemented in the program Octave [22].

2. For each $\phi \in [\alpha, \beta]$ and a given time t, we calculate the value $\varphi(\phi, t)$

3. Given the mapping $y = \varphi(\phi, t)$, we numerically estimate the PDF $\psi(y)$ from a given histogram constructed from the randomly generated trajectories.

4. Finally the histogram needs to be properly normalised.

3.4.2 The FDF-algorithm

Here we will use x rather than ϕ as a random variable, to stress the fact that the theory also works for non-invertible functions, which are not solutions of any RDE. We will restrict the use of ϕ for the cases where the mapping is obtained from a RDE. Again, for mappings arising from RDE, the function $g(x) = \varphi(\phi, t)$, in agreement with the notation of Section 3.2.

In the following, we list the steps of the FDF algorithm:

1. First of all we split the interval $[\alpha, \beta]$ into $N := N_{\text{div}}$ subintervals of equal length and set
$$x_i := \alpha + i\frac{\beta - \alpha}{N}, \quad i = 0, \ldots, N,$$
so that $\alpha = x_0$ and $\beta = x_N$. Then we compute the image values $g(x_i)$ either analytically or numerically.

2. Next, we consider the indexes $i \geq 1$ such that
$$(g(x_i) - g(x_{i-1}))(g(x_{i+1}) - g(x_i)) \leq 0. \tag{3.1}$$
Clearly, if i is such that the above relation is satisfied, then an extremum point of g is contained in the open interval $]x_{i-1}, x_{i+1}[$ and it will be approximated by x_i. These, together with α and β are the points α_j in Section 3.2.1.

   The algorithm saves the $(k+1)$-tuple $(\alpha_j)_{j=0,\ldots,k}$, the values $g(\alpha_j)$, together with the set of j-indices is the set of i's such that (3.1) holds. At this point, also the vector $\Lambda = (\lambda_1, \ldots, \lambda_k)$ and the $(k+1)$-tuple $(m_j)_{j=0,\ldots,k}$ are determined, together with the range $[g_{\min}, g_{\max}]$ of the function g.

3. In order to produce the ordered set $B = \{b_0, \ldots, b_\ell\}$ with $g_{\min} = b_0 < b_1 < \cdots < b_\ell = g_{\max}$, we sort the values $g(\alpha_j)$ in increasing order and erase the possible repeated values (if any). At this step, also the central points $c_i = \frac{b_{i-1}+b_i}{2}$ are determined and then find the set of indices $I(c_i) = I(y)$, for all $y \in]b_{i-1}, b_i[$. In fact, we have that $j \in I(c_i)$ if and only if
$$0 < (c_i - g(\alpha_{j-1}))\text{sign}(\lambda_j) < |\lambda_j|,$$

according to (3.2). This procedure allows to save the set $I(c_i)$. In a similar manner, we determine the sets $I(b_i)$.

4. The function η is approximated with a piecewise linear interpolant passing through the points $(\hat{g}(x_i), x_i)$ where the values $\hat{g}(x_i)$ are computed using (3.1).

5. As a last step, we divide each interval $[b_{i-1}, b_i]$ into a finite number of parts with a fixed step-size Δ (in this manner the larger intervals are divided into larger parts than the smaller ones). Then, knowing the sets $I(b_{i-1}, I(c_i), I(b_i)$ and using (3.3), we can determine the values $u_{\rho_1}(y), \ldots, u_{\rho_p}(y)$ (where, in this case we have $\{\rho_1, \ldots, \rho_p\} = I(y)$), for each y in the Δ-partition of $[b_{i-1}, b_i]$. From these points we find the images $\eta(u_{\rho_1}(y)), \ldots \eta(u_{\rho_p}(y))$ in $[\alpha, \beta]$ and finally we can easily compute

$$\mu_Y(y) = \sum_{i \in I(y)} \mu_X(\eta(u(y))) \frac{d\eta}{du}(u(y)).$$

Observe that, in the algorithm, the derivative of η, can be easily obtained either with the absolute value of $1/g'\eta(u(y))$ (when the analytic expression of g is known), or by a standard approximation of the incremental ratio of g computed by a subroutine in the differential equation solver.

3.5 Numerical results

In this section we provide some numerical experiments that show the feasibility and reliability of our theory. For the initial random variable X, let us choose the non-uniform, non-gaussian density function

$$\mu_X(x) = \frac{\sin(\omega x) + 2}{\int_\alpha^\beta (\sin(\omega x) + 2) dx}, \quad \omega = 5. \tag{3.1}$$

which we will use the same for all the examples. Clearly, $\mu_X(x) \geq 0$ for all $x \in [\alpha, \beta]$ and $\int_\alpha^\beta \mu_X(x) dx = 1$.

3.5.1 Example (a)

As a first example, we analyze the logistic map $L(x) = rx(1-x)$, described in the case (a) in the Introduction, and study the third iterate $g(x) := L^{(3)}(x)$, which is analogous to fixing a final time in a physical map, although this example is a case

in which the mapping is not created from a RDE. We thus brush the interval of initial values $x \in [\alpha, \beta]$ to generate the function $g(x)$. In agreement with the case presented in Figure 3.1, we take $r = 3.9$. The natural domain is then the interval $[\alpha, \beta] = [0, 1]$. Moreover, $g_{\min} = 0$ and $g_{\max} = L(1/2) = r/4 = 0.975$. For the simulation, we have chosen $N = N_{\text{div}} = 400$.

Figure 3.12 shows the density μ_X and the function g. Figure 3.13 shows the func-

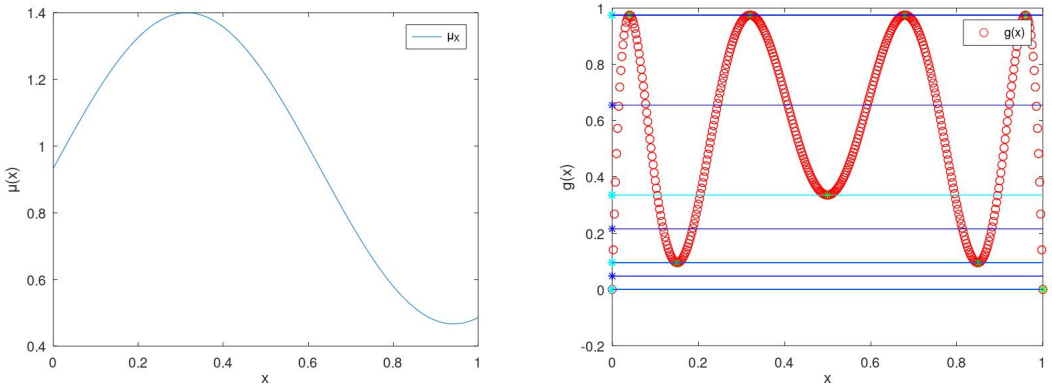

Figure 3.12: For the above set of parameters, we consider the density function μ_X (left panel) and the function g (right panel). In the graph of function g we have marked, on the vertical axis, the points $b_0, \ldots, b_\ell$, making the set B (of four points), together with the three middle points c_i. From the figure, the meaning of Lemma 2 is evident.

tion η (which is the inverse of $\hat{g}$) and the resulting density function μ_Y, produced numerically via both the brute-force technique and the FDF-A, for comparison. It is apparent from the figure that our approach provides a smoother, more precise outcome than the brute-force one. Also very important is that with the FDF-A the computational cost is remarkably reduced. This is particularly relevant when the number if iterates is very large. In the Monte Carlo approach, the generation of the bundle of trajectories may become a computationally very intensive task.

3.5.2 Example (b)

As a second example, we consider a projection of the Poincaré map associated with the shooting method applied to a second-order scalar equation of Duffing type $x'' + \rho(x) = 0$. With reference to the two cases introduced in Figure 3.2 and Figure 3.3, we study the "classical" Duffing equation with $\rho(x) = 4x^3$ and the pendulum equation with $\rho(x) = \sin(x)$.

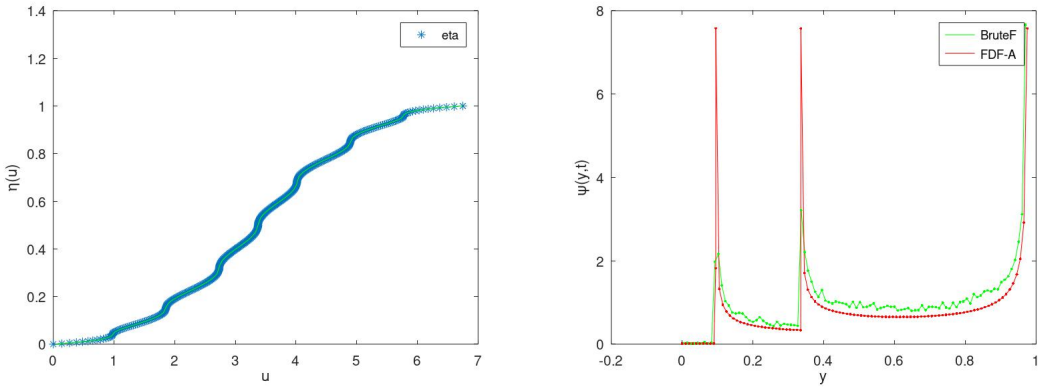

Figure 3.13: The function η (left panel) and the density function μ_Y (right panel). For the density function we compare two different graphs obtained, respectively, by the brute-force algorithm (in green) and by the FDF-A (in red).

For the former case, we take as reference time-interval $[0, T_{\max}] = [0, 5]$ and solve the initial value problems

$$\begin{cases} y' = v,\ v' = -4y^3 \\ y(0) = 0,\ v(0) = \phi \end{cases} \tag{3.2}$$

on the interval $[0, T_{\max}]$, to obtain the function $\phi \mapsto y(t, \phi)$ for $t = T_{\max}$ (cf. Figure 3.2, lower panel). To solve numerically (3.2) we use an already implemented ODE-solver of Octave [22], with a step-size 5/300. The chosen density function μ_X is the same as in (3.1) for the interval $[\alpha, \beta] = [0, 5]$. Moreover, $g_{\min} \approx -1.3015$ and $g_{\max} \approx 1.6717$. For the simulation, we have chosen $N = N_{\text{div}} = 300$.

Figure 3.14 shows the density μ_X and the function $g(x) = y(t, x)$. Figure 3.15 shows the function η and the resulting density function μ_Y, numerically produced via the brute-force technique and also through the FDF-A.

Again, the results obtained with the FDF algorithm are smoother, more accurate and are produced at lower computational cost than with the brute-force algorithm.

Considering now the case of the pendulum equation, we take as reference time-interval $[0, T_{\max}] = [0, 18]$ and solve the initial value problems

$$\begin{cases} y' = v,\ v' = -\sin(y) \\ y(0) = 0,\ v(0) = \phi \end{cases} \tag{3.3}$$

on the interval $[0, T_{\max}]$, obtaining the function $\phi \mapsto y(t, \phi)$ for $t = T_{\max}$ (cf. Figure 3.3, right panel). To solve numerically (3.3) we use, as in the above example,

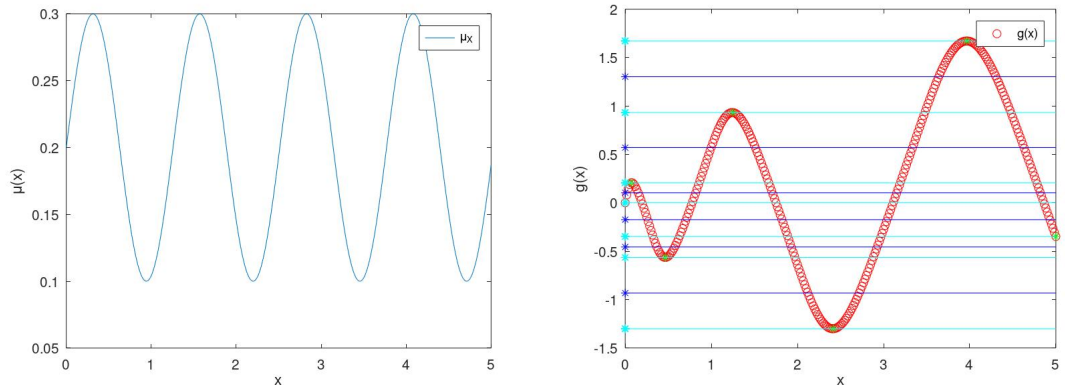

Figure 3.14: For the above set of parameters, we consider the density function μ_X (left panel) and the function g (right panel). In the graph of function g we have marked, on the vertical axis, the points $b_0, \ldots, b_\ell$, making the set B (of seven points), together with the six middle points c_i.

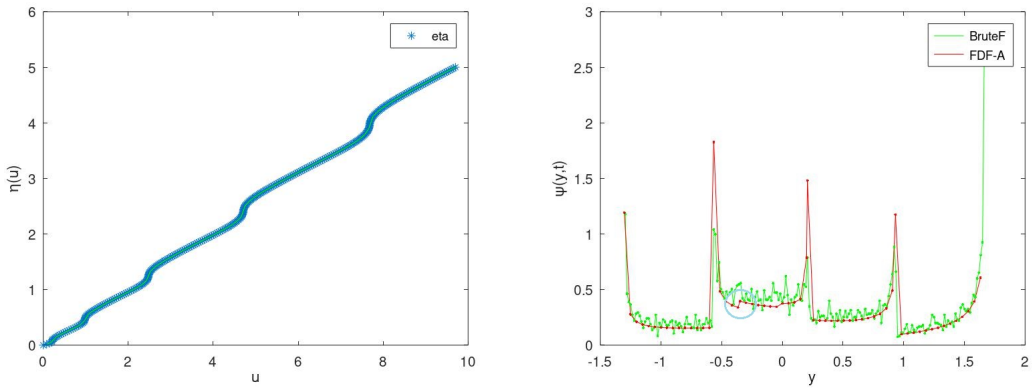

Figure 3.15: The function η (left panel) and the density function μ_Y (right panel). For the density function we compare two different graphs obtained, respectively, by the brute-force algorithm (in green) and by the FDF-A (in red).

an already implemented ODE-solver of Octave [22], with a step-size 18/200. The chosen density function μ_X is the same as in (3.1) for the interval $[\alpha, \beta] = [0, 1.99]$. Moreover, $g_{\min} \approx -2.5019$ and $g_{\max} \approx 2.9224$. For the simulation, we have chosen $N = N_{\text{div}} = 200$.

Figure 3.16 shows the density μ_X and the function $g(x) = y(t, x)$.

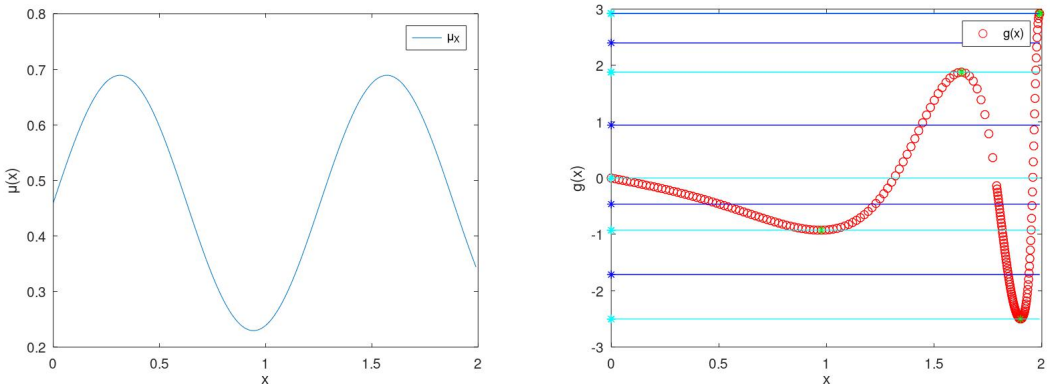

Figure 3.16: For the above set of parameters, we consider the density function μ_X (left panel) and the function g (right panel). In the graph of function g we have marked, on the vertical axis, the points $b_0, \ldots, b_\ell$, making the set B (of five points), together with the four middle points c_i.

Figure 3.17 shows the function η and the resulting density function μ_Y, produced, numerically, via the brute-force technique and the FDF-A.

3.5.3 Example (c)

As a third example, we consider the problem in (3.9), leading to an explicit form for $\varphi(\phi, t)$ as in (3.10). In this case, we have an explicit known form for the function

$$g(x) = kx + A\cos(\omega t + x), \tag{3.4}$$

where, k, A, ω, t are fixed parameters for our numerical simulation. The chosen density function μ_X is the same as in (3.1) for the interval $[\alpha, \beta] = [2, 4]$. For the simulation, we have chosen $N = N_{\text{div}} = 200$.

Figure 3.18 shows the density μ_X and the function g, with g defined for the parameters $k = 1$, $A = 2$, $\omega = 6$ and $t = 1$.

Figure 3.19 shows the function η (which is the inverse of $\hat{g}$) and the resulting density function μ_Y, via the brute-force procedure as well as the FDF-A.

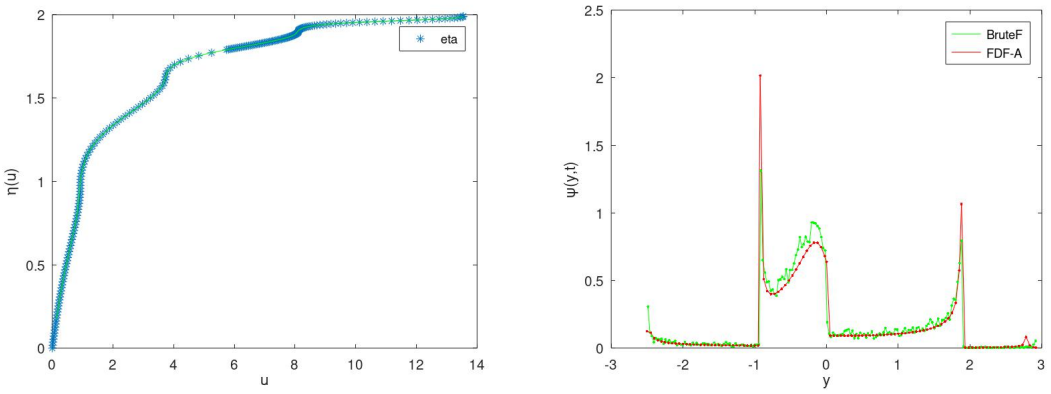

Figure 3.17: The function η (left pannel) and the density function μ_Y (right pannel). For the density function we compare two different graphs obtained, respectively, by the brute-force algorithm (in green) and by the FDF-A (in red).

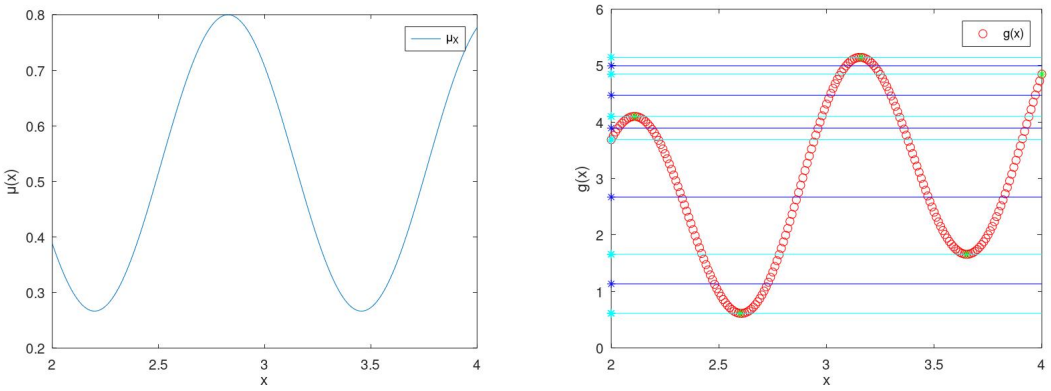

Figure 3.18: We consider the density function μ_X (left panel) and the function g (right panel). In the graph of function g we have marked, on the vertical axis, the points $b_0, \ldots, b_\ell$, making the set B (of six points), together with the five middle points c_i. From the figure, the meaning of Lemma 2 is evident.

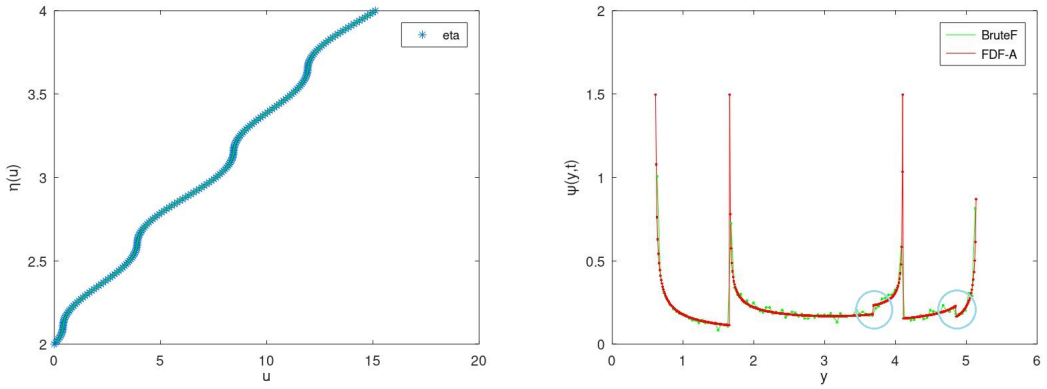

Figure 3.19: The function η (left panel) and the density function μ_Y (right panel). For the density function we compare two different graphs obtained, respectively, by the brute-force algorithm (in green) and by the FDF-A (in red). It is apparent that our approach provides a smoother and more precise outcome than the other one. Moreover, with the FDF-A the computational cost is remarkably reduced.

Finally, we want to point out the small jumps present in Figure 3.15 and Figure 3.19 which we have highlighted with a small circle. These discontinuities are due neither to numerical errors nor to any flaw in the FDF algorithm. Instead, they reflect the complexity of the overlapping of different branches in the folded domain, as we have shown in the sketch of Figure 3.11. In this particular case, they are due to the overlapping of the extremal points $g(\alpha)$ and/or $g(\beta)$ with other values in the image set $g(]\alpha, \beta[)$.

3.6 Conclusion and future work

In the present paper we have addressed a classical problem in the study of random variables, namely, quoting [4, p.80]: *Let X be a RV with density f. Suppose $Y = g(X)$. Can we express the density of Y (if it exists), in terms of f ?* If X has a continuous density function and g is piecewise strictly monotone and continuously differentiable, the problem is solved, from a theoretical point of view, by the formula

$$\mu_Y(y) = \sum_{i=1}^{n} \mu_X(h_i(y))|h_i'(y)|\mathbb{1}_{\wedge}(y) \tag{3.1}$$

(see [4, Corollary 11.3]). In (3.1), $\wedge$ denotes the range of g and it is assumed that there exists intervals $I_1, I_2, \ldots, I_n$ which partition the domain of g and such that

g is strictly monotone and continuously differentiable on the interior of each I_i. Then, $h_i : g(I_i) \to I_i$ denotes the inverse of g restricted to I_i . In applying the above formula, one has to decide *for every y in the range of g* the correct functions h_i to be chosen in the summation. In the simplest case, g is continuously differentiable with non-vanishing derivative, and the above formula reduces to

$$\mu_Y(y) = \mu_X(h(y))|h'(y)|, \quad \text{for } \; h = g^{-1} \tag{3.2}$$

(see [4, Corollary 11.2]). This latter result may be easily extended to the vector case; in this situation, one has to assume that g is a diffeomorphism.

Applications of (3.2) for one-dimensional and higher-dimensional models have received a great deal of interest in the past decades, as witnessed by a growing list of published research articles in this area in recent years (see, for instance, Refs. [9, 8, 15, 6, 7, 10, 18]). Actually, the implementations of (3.2) in applied mathematical models is usually referred to as *Probabilistic Transformation Methods* (according to Kadry in [17]) or *Random Variable Transformation (RVT) Technique* (according to Casabán et al. in Ref. [15] and also to the more recent work by Cortés et al. [19]). Further applications of this method have been developed for various mathematical model equations of great interest for ecological and biological sciences in subsequent articles, as those cited above. In some of these articles (as, for instance, in Ref. [6]) the domain of the inverse transformation is split into two disjoint open intervals, so that (3.1) simplifies to equation (3.2) applied twice. In the very recent work [16], Almalki, Elshekhipy and Almutairi deal with a very general case of non-monotone transformation g and study the probability distribution of $Y = g(X)$ from a theoretical and numerical point of view.

Our work, independently follows a similar line of reasoning, namely, to obtain information of the RV $Y = g(x)$, under the most general assumptions for g. With this respect, our main contributions in the present work are the following:

- As already observed, in applying the formula (3.1), one has to decide *for every y in the range of g* the correct functions h_i to choose in the summation. With our approach (and using Lemma 1 and Lemma 2) rather we can easily determine the index set $I(y)$ associated with y;

- We have proposed a new method to obtain the piecewise-partial inverses h_i of g, by introducing a unique global function η. The function η, in some sense, "unfolds" the graph of g in a manner such that the derivatives (in absolute value) $|h_i'(y)|$ in (3.1) correspond to the inverse derivative of η computed in different intervals.

- Our approach is mathematically rigorous, because we can independently re-establish (3.1), passing through the use of the function η (see Section 3.2.1);

- Our method, when numerically implemented, requires a minimal set of information and therefore is extremely simple and fast compared to standard histogram methods based on a Monte Carlo sampling of the initial probability distribution.

The very recent articles [16, 19, 21, 20] show the persistent interest and relevance of the problem considered in this work, both from the theoretical and the applied point of view. We hope that our contribution can provide a new tool in this area of research.

As a final comment, we outline some possible extensions of our approach to the higher-dimensional case. Let X be a m-dimensional random variable with domain $\mathfrak{D}_X$ and let $g : \mathbb{R}^m \to \mathbb{R}^m$ be continuously differentiable mapping, leading to the new Random Variable $Y = g(X)$, with values in $\mathbb{R}^m$. As in the one-dimensional case, we are interested in providing an efficient method to estimate the probability density function μ_Y in terms of μ_X. From a theoretical point of view, the problem is solved by [4, Corollary 12.1]; however, implementing the method in concrete examples may be a formidable task. This is therefore a problem of great interest, as witnessed by the recent articles [20, 21]. As Lemma 1 and Lemma 2 can be proven to be also valid in more than one dimension, our algorithm can be extended to maps connecting higher dimensional spaces (see also Remark 1). On the other hand, while in the one-dimensional case, the singular set reduces to a finite (discrete) set of points, in dimension $m \geq 2$, we have to face some complex differential geometry problems concerning the boundaries of the sets where g is partially invertible. This problem will be addressed next.

Bibliography

[1] Balibrea, F. and Caraballo, T. and Kloeden, P. E. and Valero, J. **Recent developments in dynamical systems: three perspectives**. *International Journal of Bifurcation and Chaos in Applied Sciences and Engineering* **2010**, *20,9*, 2591–2636.

[2] Arnold, L. **Random dynamical systems**. *Springer Monographs in Mathematics*, Springer-Verlag, Berlin, **1998**.

[3] Soong, T. T. **Random differential equations in science and engineering**. *Academic Press [Harcourt Brace Jovanovich, Publishers], New York-London* **1937**, Mathematics in Science and Engineering, Vol. 103.

[4] Jacod, J. and Protter, P. **Probability essentials**. *Universitext, Springer-Verlag, Berlin* **2000**.

[5] Papoulis, A. **Probability, random variables, and stochastic processes**. *McGraw-Hill Series in Electrical Engineering. Communications and Information Theory* **1984**, McGraw-Hill Book Co., New York.

[6] Casabán, M.-C. and Cortés, J.-C. and Navarro-Quiles, A. andì Romero, J.-V. and Roselló, M.-D. and Villanueva, R.-J. **Probabilistic solution of the homogeneous Riccati differential equation: a case-study by using linearization and transformation techniques**. *Journal of Computational and Applied Mathematics* **2016**, *291*, 20–35.

[7] Casabán, M.-C. and Cortés, J.-C. and Navarro-Quiles, A. and Romero, J.-V. and Roselló, M.-D. and Villanueva, R.-J. **A comprehensive probabilistic solution of random SIS-type epidemiological models using the random variable transformation technique**. *Communications in Nonlinear Science and Numerical Simulation* **2016**, *32*, 199–210.

[8] Calatayud, J. and Cortés, J. C. and Dorini, F. A. and Jornet, M. **Dealing with variability in ecological modelling: an analysis of a random**

non-autonomous logistic population model. *Mathematical Methods in the Applied Sciences* **2022**, *45,6*, 3318–3333.

[9] Burgos, C. and Calatayud, J. and Cortés, J.-C. and Navarro-Quiles, A. **A full probabilistic solution of the random linear fractional differential equation via the random variable transformation technique**. *Mathematical Methods in the Applied Sciences* **2018**, *41,18*, 9037–9047.

[10] Casabán, M.-C. and Cortés, J.-C. and Romero, J.-V. and Roselló, M.-D. **Solving random homogeneous linear second-order differential equations: a full probabilistic description**. *Mediterranean Journal of Mathematics* **2016**, *13,6*, 3817–3836.

[11] Li, T. Y. and Yorke, J. A. **Period three implies chaos**. *American Mathematical Monthly* **1975**, *82,10*, 985–992.

[12] Murray, J. D. **Mathematical biology. I**. *Interdisciplinary Applied Mathematics, Springer-Verlag, New York* **2002**.

[13] Hale, J. K. **Ordinary differential equations**. *Robert E. Krieger Publishing Co., Inc., Huntington, N.Y.* **1980**.

[14] Ambrosetti, A. and Prodi, G. **A primer of nonlinear analysis**. *Cambridge Studies in Advanced Mathematics* **1995**, *34*.

[15] Casabán, M.-C. and Cortés, J.-C. and Romero, J.-V. and Roselló, M.-D. **Determining the first probability density function of linear random initial value problems by the random variable transformation (RVT) technique: a comprehensive study**. *Abstract and Applied Analysis* **2014**, Art. ID 248512, 25.

[16] Almalki, N. H. and Elshekhipy, A. A. and Almutairi, I. S. **A numerical modeling and its computational implementing simulation for generating distributions of the complicated random variable transformations with applications**. *Applied Numerical Mathematics. An IMACS Journal* **2023**, *186*, 274–288.

[17] Kadry, S. **On the generalization of probabilistic transformation method**. *Applied Mathematics and Computation* **2007**, *190,2*, 1284–1289.

[18] Cortés, J.-C. and El-Labany, S. K. and Navarro-Quiles, A. and Selim, M. M. and Slama, H. **A comprehensive probabilistic analysis of approximate SIR-type epidemiological models via full randomized discrete-time**

Markov chain formulation with applications. *Mathematical Methods in the Applied Sciences* **2020**, *43,14*, 8204–8222.

[19] Cortés, J.-C. and López-Navarro, E. and Romero, J.-V. and Roselló, M.-D. **Probabilistic analysis of a cantilever beam subjected to random loads via probability density functions**. *Computational & Applied Mathematics* **2023**, *42,1*, 32.

[20] Navarro-Quiles, A. and Laudani, R. and Falsone,G. **A new stochastic method based on the Taylor expansion to compute response probability densities of uncertain systems**. *International Journal for Numerical Methods in Engineering* **2023**, *124,5*, 1111–1127.

[21] La Valle, G. and Laudani, R. and Falsone, G. **Response probability density function for non-bijective transformations**. *Communications in Nonlinear Science and Numerical Simulation* **2022**, *107*, Paper No. 106190, 9.

[22] J. W. Eaton and D. Bateman and S. Hauberg and R. Wehbring **GNU Octave version 7.3.0 manual: a high-level interactive language for numerical computations**. *https://www.gnu.org/software/octave/doc/v7.3.0/* **2022**.

Chapter 4

Conclusions and future work

4.1 Conclusions

This thesis is divided into two well-defined parts. Here, in the last section, we provide the most important conclusions that can be drawn from each part.

The first research topic developed in this thesis deals with the application of Artificial Intelligence (AI) to the parametrization of a Flory-Huggins (FH) model from experimental data. We analysed the phase diagram of ternary solutions of gelatin, maltodextrin and water at 50° C. The ternary system studied in this thesis is particularly relevant for the formation of water/water emulsions and gelatin microgels. Notice that this contribution has a double interest. Firstly, the importance of our work is major because the two-phase region is of particular interest in the preparation of colloidal dispersions in gelatin/maltodextrin aqueous mixtures for which our contribution constitutes a tool to guide the set up for its industrial production. Secondly, our work, despite being less obvious, presents a challenging speculation about modelling chemical experiments. Artificial intelligence applied to the experimental phase diagram was used to propose a new method for determining the optimal Flory-Huggins parameters. By training a Neural Network providing only the number of phases for each experimental point, generated from a Flory-Huggins model, it is possible to predict the FH parameters that best describe the chemical experiments. In particular, we numerically created a large number of state points with an algorithm based on the FH model, for arbitrary FH parameters and keep only whether a state point contained one or two phases. We trained the NN with this numerically generated data to ultimately feed the NN with the experimental phase diagram to produce the optimal parameters consistent with the phase diagram of the physicochemical experiments. We point out that the experimental data we had did not provide us with knowledge about the

compositions of the coexisting phases at each starting point. These compositions and tie-lines can be inferred using the predicted FH parameters. We warn the reader that applying such a method requires knowledge of the phase boundaries of the experimental data to feed the NN. Notice that the experimental knowledge of the compositions of the phases in equilibrium would have provided a sounder fit for the FH parameters using standard methods. The ultimate importance of the procedure followed in this work is that we obtained the parametric fit with a very limited information, contained in the location of the phase boundary. The use of a NN has allowed us to extract this information as a function of the FH parameters. Consequently, the application of the proposed method is strongly bound to the quality of such experimental phase boundaries. Although this sensitivity to the quality of the experiments affects this method, we observed that our work is able to find a reasonable fit of the phase diagram, including reasonable estimates of the *a priori* unknown phase compositions at the experimental points. Our predicted compositions have been compared to Raman spectroscopy experiments and we obtained more than a reasonable agreement, which confirms the last statement. In view of all these results, our work is expected to be of help in determining the conditions for the formation of nanostructured systems developed with phase separation of ternary solutions of gelatin, maltodextrin and water. What makes our contribution even more fascinating is that it offers a new method to predict the FH parameters of solutions that contain two or more polymers.

The second research topic developed in this thesis constitutes a much more theoretical analysis, when compared with the first one. However, the underlying philosophy that motivates this thesis remains unchanged. Indeed also the second part of the work aims at providing a computational tool targeting applied sciences and engineering. Furthermore, also the second part has been originated trying to connect different fields of knowledge like pure Mathematics and Computational Physics. To be more specific, in the second part of the thesis we address a classical problem of Probability theory which has a huge interest for Computational Physics and Statistics. In particular, we developed a novel mathematical concept, called Folding Domain Function (FDF), which solves the classical task of the *Random Variable transformation (RVT) problem* in a very efficient way. This problem concerns the transformation of a Random Variable (RV) X into a new RV $Y = g(X)$ through a function g that acts as a mapping $X \to Y$. As already mentioned, this is a very old problem and its solution is well-known for the case in which the function g is invertible, as the probability distribution of Y can be obtained from that of X by stating

$$P(Y) = \int dX\, \delta(Y - g(X)) P(X)$$

The analytical evaluation of the right-hand side of this equation requires the knowledge of $g^{-1}(Y)$. Hence, for this case a well-known formula can be applied to get the new probability distribution for the mapped RV Y. Although the classical theory of Probability ensures that the problem can be solved also in the case when g is not invertible, there is a lack of methodologies to solve this more complex case in the literature. Our contribution, along with the FDF theoretical description of the problem, enables us to implement an algorithm that is both highly effective and cost-effective. The reason why this second project is so interesting is because it addresses a very general problem (the RVT problem) that has many applications in Statistics, Probability, Physics, among others. We deal with Random Differential Equations (RDEs) which are a special class of Stochastic Differential Equations (SDEs) in which randomness affects only initial data. As we discussed in the work, determining the solution of an RDE requires to solve an RVT problem, where the transformation function g is the solution of an Ordinary Differential Equation (ODE). Consequently, our FDF method can be applied to generate a very fast algorithm that determines the Probability Distribution Function (PDF) of the new RV $Y = g(X)$. We stress that the knowledge of an analytical expression of the function g is not required within the FDF algorithm. This feature makes our contribution very competitive. Indeed, most of the ODEs that arise in this type of physical problems do not admit an analytical solution g which can be only determined in a finite set of values by applying some *Numerical Integrators methods*. Furthermore, in most of the cases of interest in Physics, the complexity of the system gives rise to an RDE that can be transformed into an RVT problem characterised by a transformation function g that is non invertible. These two last aspects make our contribution relevant and timely to solve many RVT problems of interest in given applications.

4.2 Future Work

The first project presented in this thesis can be continued by replicating the proposed method for determining the Flory Huggins parameters of numerous polymer mixtures. However, the natural next step is to use concentration data to train a NN, as it numerically available in the solution of the phase diagram for each set of FH parameters. Hence, if the experimental data on the system gelatin-maltodextrin-water were available, we could test the application of the method to fit the parameters and compare the obtained data with the experimental compositions, as the latter is the relevant information regarding the possible applications of the system under study.

Regarding the second project presented in this thesis, we have a long list of pos-

sible continuations of the presented work. In particular, from the theoretical point of view, we can develop an extension of the model to cases of higher dimensions. Indeed we recall that our FDF method is able to solve the RVT problem in the one dimensional case (i.e. the transformation function $g : [\alpha, \beta] \subset \mathbb{R} \to \mathbb{R}$ is a real function of real variable). Then a challenging and interesting research project will be to find either an extension of the FDF model to higher dimension cases or to adapt the one dimensional case to these type of generalizations. To be more specific we may adapt the FDF method to solve a RVT problem in which we have a random vector $(X_1, \ldots, X_N)$ of random variables that is transformed into a new one dimensional RV $Y = G(X_1, \ldots, X_N)$. We notice that in such a case the transformation function is a *scalar field* $G : [\alpha_1, \beta_1] \times \cdot \times [\alpha_N, \beta_N] \subset \mathbb{R}^N \to \mathbb{R}$. This case corresponds to the physical problem of having an observable y (that will be described by a RV Y) that depends on $N \in \mathbb{N}$ random variables or parameters $x_1, \ldots, x_N$ (that will be described by a random vector $(X_1, \ldots, X_N)$). A further theoretical problem of great interest is to extend the method for problems in which we have also multiple observables $Y_1, \ldots, Y_M$ with $(M \in \mathbb{N})$. In this more complex case, the transformation function is a *vector field* $\vec{G} : [\alpha_1, \beta_1] \times \cdot \times [\alpha_N, \beta_N] \subset \mathbb{R}^N \to \mathbb{R}^M$. Alternatively we can develop more concrete research projects by applying the 1-dimensional the FDF method, as it stands, to specific 1-dimensional cases of interest in Physics (either the ones developed in chapter 2 or the these developed in the papers quoted therein). In conclusion we hope that the two research projects, developed in this thesis, may provide some helpfully tools for future research and they can be inspiring contributions for future speculations.

List of Papers

- Fabrizio Masullo, Yoran Beldengrün, Jonathan Miras, Allan D. Mackie, Jordi Esquena, Josep Bonet Avalos, **Phase behavior of gelatin/maltodextrin aqueous mixtures studied from a combined experimental and theoretical approach,** *Fluid Phase Equilibria* Volume 524, 1st of December 2020, 112675.

- Fabrizio Masullo, Fabio Zanolin, Josep Bonet Avalos, **Folding Domain Functions: a Random Variable Transformation technique for the non-invertible case, with applications to REDs,** *Communications in Nonlinear Science and Numerical Simulation* (under review).

Appendix A

Supporting Information

In this appendix we provide the supporting information related to the experimental data on the samples of gelatin-maltodextrin mixtures of Chapter 2. The information is listed below.

- Light transmission, measured by using the Turbiscan, of data of some samples.
- Two tables containing the Flory-Huggins parameters for the numerical experiments used to construct the training set, for the pH 5 case (set 1 and set 2).
- Table containing compositions, obtained with the best FH parameters, for the pH 5 case (set 1).
- Table containing compositions, obtained with the best FH parameters, for the pH 5 case (set 2).
- Table containing the Flory-Huggins parameters for the numerical experiments used to construct the training set, for the pH $3-4$ case.
- Table containing compositions, obtained with the best FH parameters, for the pH $3-4$ case.

A.1 Light transmission, measured by using the Turbiscan, of data of some samples.

The light transmission data of some samples, prepared in compositions within the three-phase $L_1 + L_2 + S$ region, was acquired for a period of 5 days. Measurements of multiple light scattering were performed using a Turbiscan apparatus, at 50°C constant temperature, operating with near infrared light (λ=880 nm). The variations of transmittance were followed as a function of time, for various positions of the sample, including the liquid-liquid interphase and the bottom of the samples. Results of light transmission are shown in Figure A.1. The four samples analysed were 8 %Gel/10 %MD and 12 %Gel/8 %MD, in which the gelatin-rich phase had a bigger volume fraction, and 3 %Gel/20 %MD and 4 %Gel/1 %MD, with a larger volume fraction for the maltodextrin-rich phase. Light transmission

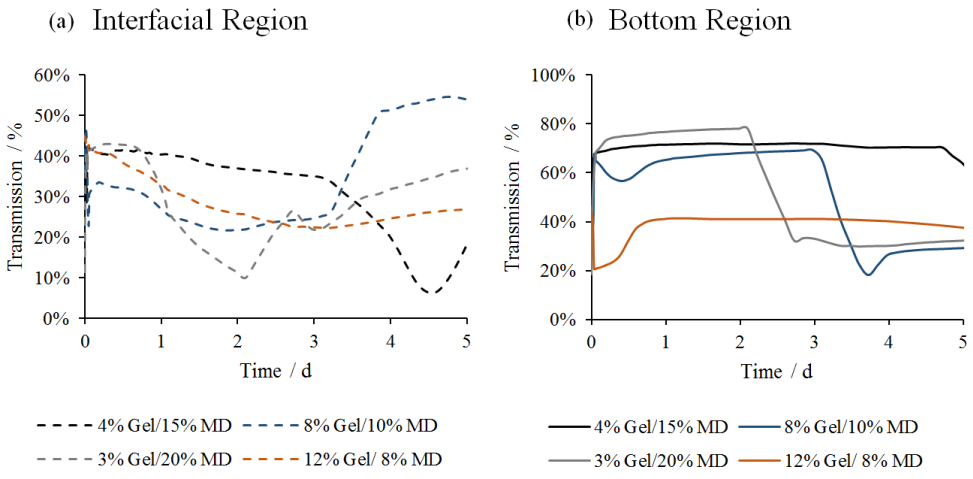

Figure A.1: Light transmission, measured by using the Turbiscan apparatus, shows the formation of solid particles in four different gelatin/maltodextrin mixtures, which phase separate into two liquid phases. (a) shows transmission of the sample at the liquid-liquid interphase, (b) transmission at the bottom of the sample.

shows an initial decrease in the interfacial region, reaching a minimum that is followed by a recovery in transmission. By contrast, in the bottom of the vials, light transmission shows a sharp reduction at certain times. In the interfacial region, the initial decrease in transmission is probably due to formation of solid particles around the interfacial region, as visually observed by naked eye. After the mini-

mum, transmission increases, which is probably caused by the detachment of solid particles from the interface and sedimentation of such particles on the bottom of the vials. In contrast, light transmission in the bottom shows a sharp decrease, which certainly is due to the formation of a sedimentation layer, as also visually observed by naked eye. The velocity of sedimentation clearly depends on sample composition. For example, sample with 12 wt% gelatin and 8 wt% maltodextrin displays a fast precipitation, whereas a much slower precipitation is observed in the sample with 4 wt% gelatin and 10 wt% maltodextrin, which requires more than 5 days to reach equilibrium. In conclusion, the above results demonstrate that the particles form in the interfacial region and later they sediment, producing a layer on the bottom of samples.

A.2 Estimated compositions of the phases

Num. exp.	χ_{12}	χ_{13}	χ_{23}
1	0.1000	0.7000	0.9750
2	0.1500	0.7000	0.9000
3	0.1500	0.6000	0.9000
4	0.1000	0.7500	1.0000
5	0.2000	0.7500	1.0000
6	0.0500	0.6000	0.8000
7	0.0500	0.8000	0.9500
8	0.1500	0.7500	0.9000
9	0.1500	0.7000	0.8000
10	0.2000	0.7000	0.9000
11	0.2000	0.6500	0.8000
12	0.1000	0.6000	0.8000
13	0.1500	0.6000	0.8000
14	0.3000	0.9000	1.2000
15	0.4500	0.7000	0.7200
16	0.5000	1.0000	1.3000
17	0.4000	0.9000	1.2000
18	0.5000	1.0000	1.2000
19	0.5000	0.9000	1.3000
20	0.4000	1.0000	1.2000
21	0.4500	0.9500	1.2500
22	0.4500	0.9000	1.2000
23	0.4500	0.9000	1.2500
24	0.4500	1.0000	1.2000
25	0.3500	1.0000	1.3000
26	0.3500	0.9000	1.3000

Table A.1: Flory-Huggins parameters for the numerical experiments used to construct the training set for pH 5 (set 1 and set 2)

PH 5 case						
sample	starting composition		dilute phase		dense phase	
number	ϕ_2	ϕ_3	ϕ_2	ϕ_3	ϕ_2	ϕ_3
1	0.0034	0.1618	0.0953	0.0080	$< 10^{-4}$	0.1674
2	0.0033	0.1182	0.0792	0.0103	$< 10^{-4}$	0.1228
3	0.0033	0.1294	0.0836	0.0096	$< 10^{-4}$	0.1343
4	0.0033	0.0634	0.0477	0.0163	$< 10^{-4}$	0.0668
5	0.0037	0.0484	0.0328	0.0200	0.0001	0.0518
6	0.0038	0.0962	0.0694	0.0119	$< 10^{-4}$	0.1010
7	0.0051	0.0780	0.0600	0.0137	$< 10^{-4}$	0.0839
8	0.0070	0.0644	0.0518	0.0154	$< 10^{-4}$	0.0720
9	0.0075	0.0852	0.0660	0.0126	$< 10^{-4}$	0.0944
10	0.0076	0.1082	0.0775	0.0106	$< 10^{-4}$	0.1188
11	0.0078	0.0421	0.0209	0.0222	0.0002	0.0493
12	0.0079	0.0741	0.0595	0.0138	$< 10^{-4}$	0.0833
13	0.0080	0.0502	0.0397	0.0182	$< 10^{-4}$	0.0582
14	0.0089	0.0966	0.0730	0.0113	$< 10^{-4}$	0.1084
15	0.0145	0.0640	0.0578	0.0141	$< 10^{-4}$	0.0806
16	0.0146	0.0741	0.0646	0.0128	$< 10^{-4}$	0.0919
17	0.0144	0.0491	0.0453	0.0168	$< 10^{-4}$	0.0641
18	0.0147	0.0386	0.0339	0.0197	$< 10^{-4}$	0.0528
19	0.0152	0.0705	0.0628	0.0132	$< 10^{-4}$	0.0887
20	0.0154	0.0844	0.0711	0.0117	$< 10^{-4}$	0.1044
21	0.0222	0.0787	0.0728	0.0114	$< 10^{-4}$	0.1081
22	0.0218	0.0352	0.0384	0.0185	$< 10^{-4}$	0.0569
23	0.0226	0.0507	0.0546	0.0148	$< 10^{-4}$	0.0759
24	0.0231	0.0638	0.0647	0.0128	$< 10^{-4}$	0.0920
25	0.0231	0.0638	0.0742	0.0111	$< 10^{-4}$	0.1111
26	0.0231	0.0638	1 phase			
27	0.0231	0.0638	0.0548	0.0148	$< 10^{-4}$	0.0761
28	0.0231	0.0638	0.0639	0.0130	$< 10^{-4}$	0.090
29	0.0036	0.0072	1 phase			
44	0.0036	0.0072	1 phase			
45	0.0041	0.0347	1 phase			
46	0.0041	0.0201	1 phase			
47	0.0072	0.0072	1 phase			
48	0.0078	0.0207	1 phase			
49	0.0081	0.0345	0.0181	0.0251	0.0015	0.0405
50	0.0149	0.0067	1 phase			
51	0.0192	0.0198	1 phase			
52	0.0218	0.0077	1 phase			
53	0.0224	0.0208	1 phase			

Table A.2: Equilibrium configurations for pH 5 (set 1)

PH 5 case						
sample	starting composition		dilute phase		dense phase	
number	ϕ_2	ϕ_3	ϕ_2	ϕ_3	ϕ_2	ϕ_3
EP1	0.03	0	1 phase			
EP2	0.04	0	1 phase			
EP3	0.05	0	1 phase			
EP4	0.06	0	1 phase			
EP5	0.07	0	1 phase			
EP6	0.08	0	1 phase			
EP7	0.09	0	1 phase			
EP8	0.1	0	1 phase			
25	0.0335	0.0660	0.0374	0.0024	$< 10^{-4}$	0.5993
26	0.0330	0.0211	$< 10^{-4}$	0.0303	0.0978	0.0029
27	0.0338	0.0383	0.0359	0.0025	$< 10^{-4}$	0.5993
28	0.0340	0.0493	0.0368	0.0025	$< 10^{-4}$	0.5993
29	0.0336	0.0072	0.0066	0.0118	0.0445	0.0052
30	0.0443	0.0215	$< 10^{-4}$	0.0353	0.1044	0.0027
31	0.0449	0.0499	0.0488	0.0027	$< 10^{-4}$	0.5994
32	0.0449	0.0391	0.0478	0.0020	$< 10^{-4}$	0.5994
33	0.0443	0.0072	0.0027	0.0150	0.0586	0.0044
34	0.0591	0.0070	$< 10^{-4}$	0.0195	0.0740	0.0037
35	0.0600	0.0361	0.0636	0.0014	$< 10^{-4}$	0.5996
36	0.0597	0.0143	$< 10^{-4}$	0.0314	0.0994	0.0028
37	0.0599	0.0211	0.0619	0.0015	$< 10^{-4}$	0.5996
38	0.0738	0.0070	$< 10^{-4}$	0.0253	0.0888	0.0032
39	0.0754	0.0276	0.0788	0.0011	$< 10^{-4}$	0.5999
41	0.0894	0.0068	0.0966	0.003	$< 10^{-4}$	0.6004
40	0.0751	0.0136	0.0107	0.0026	$< 10^{-4}$	0.0387
42	0.0916	0.0289	0.0961	$< 10^{-4}$	$< 10^{-4}$	0.6004
43	0.0940	0.0144	0.0961	$< 10^{-4}$	$< 10^{-4}$	0.6004

Table A.3: Equilibrium configurations for pH 5 (set 2)

Num. exp.	χ_{12}	χ_{13}	χ_{23}
1	0.3000	0.7000	1.0000
2	0.4000	0.8500	1.1500
3	0.3000	0.6000	1.2000
4	0.5000	1.0000	1.3000
5	0.4500	0.9500	1.2500
6	0.3000	0.7000	0.9000
7	0.2000	0.5500	1.1000
8	0.4000	0.5500	1.1000
9	0.3000	0.4500	1.1000
10	0.3000	0.5500	1.2000
11	0.2000	0.4500	1.1000
12	0.3000	0.5500	1.1000

Table A.4: FH parameters used to generate the 80 states of the phase diagram for the pH 3 case.

PH 3 case						
sample	starting composition		dilute phase		dense phase	
number	ϕ_2	ϕ_3	ϕ_2	ϕ_3	ϕ_2	ϕ_3
1	0.0180	0	1 phases			
2	0.0319	0	1 phases			
3	0.0475	0	1 phases			
4	0.0044	0.0019	1 phases			
5	0.0322	0.0033	1 phases			
6	0.0236	0.0034	1 phases			
7	0.0038	0.0036	1 phases			
8	0.0068	0.0040	1 phases			
9	0.0446	0.0046	1 phases			
10	0.0476	0.0054	1 phases			
11	0.0604	0.0061	1 phases			
12	0.0086	0.0084	1 phases			
13	0.0070	0.0107	1 phases			
14	0.0150	0.0108	1 phases			
15	0.0043	0.0112	1 phases			
16	0.0157	0.0143	1 phases			
17	0	0.0152	1 phases			
18	0.0062	0.0169	1 phases			
19	0.0106	0.0190	0.0038	0.0223	0.0203	0.0141
20	0.0077	0.0216	0.0024	0.0241	0.0248	0.0130
21	0.0037	0.0218	1 phases			
22	0	0.0284	1 phases			
23	0	0.0450	1 phases			
24	0	0.0524	1 phases			
25	0.0197	0.0065	1 phases			

Table A.5: Equilibrium configurations for pH $3-4$

PH 3 case (contd.)						
sample	starting composition		dilute phase		dense phase	
number	ϕ_2	ϕ_3	ϕ_2	ϕ_3	ϕ_2	ϕ_3
26	0.0469	0.0072	1 phases			
27	0.0620	0.0073	1 phases			
28	0.0310	0.0073	1 phases			
29	0.0804	0.0075	1 phases			
30	0.0365	0.0076	1 phases			
31	0.0223	0.0077	1 phases			
32	0.0958	0.0090	1 phases			
33	0.0362	0.0139	1 phases			
34	0.0456	0.0141	1 phases			
35	0.0442	0.0151	$< 10^{-4}$	0.0395	0.0567	0.0081
36	0.0532	0.0159	$< 10^{-4}$	0.0471	0.0684	0.0069
37	0.0395	0.0174	$< 10^{-4}$	0.0391	0.0560	0.0082
38	0.0216	0.0178	0.0008	0.0283	0.0345	0.0111
39	0.0966	0.0218	$< 10^{-4}$	0.0989	0.1198	0.0032
40	0.0487	0.0220	$< 10^{-4}$	0.0515	0.0743	0.0064
41	0.0647	0.0224	$< 10^{-4}$	0.0656	0.0905	0.0050
42	0.0167	0.0225	0.0004	0.0309	0.0402	0.0102
43	0.0354	0.0227	$< 10^{-4}$	0.0428	0.0619	0.0076
44	0.0796	0.0234	$< 10^{-4}$	0.0818	0.1059	0.0040
45	0.0252	0.0234	$< 10^{-4}$	0.0370	0.0523	0.0086
46	0.0244	0.0286	$< 10^{-4}$	0.0424	0.0613	0.0076
47	0.0156	0.0359	$< 10^{-4}$	0.0449	0.0651	0.0072
48	0.0159	0.0361	$< 10^{-4}$	0.0453	0.0657	0.0072
49	0.0395	0.0431	$< 10^{-4}$	0.0702	0.0952	0.0047
50	0.0043	0.0431	$< 10^{-4}$	0.0455	0.0661	0.0071

Table A.6: Equilibrium configurations for pH $3-4$ (cont.)

PH 3 case (contd.)						
sample	starting composition		dilute phase		dense phase	
number	ϕ_2	ϕ_3	ϕ_2	ϕ_3	ϕ_2	ϕ_3
51	0.0256	0.0435	$< 10^{-4}$	0.0599	0.0845	0.0055
52	0.0365	0.0444	$< 10^{-4}$	0.0693	0.0943	0.0048
53	0.0803	0.0450	$< 10^{-4}$	0.1130	0.1301	0.0027
54	0.0644	0.0450	$< 10^{-4}$	0.0956	0.1172	0.0034
55	0.0125	0.0446	$< 10^{-4}$	0.0522	0.0752	0.0063
56	0.0963	0.0458	$< 10^{-4}$	0.1335	0.1441	0.0021
57	0.0480	0.0457	$< 10^{-4}$	0.0807	0.1049	0.0041
58	0.0204	0.0485	$< 10^{-4}$	0.0617	0.0865	0.0054
59	0.0037	0.0566	$< 10^{-4}$	0.0589	0.0833	0.0056
60	0.1000	0.0666	$< 10^{-4}$	0.1664	0.1652	0.0015
61	0.0368	0.0662	$< 10^{-4}$	0.0950	0.1168	0.0034
62	0.0815	0.0670	$< 10^{-4}$	0.1435	0.1507	0.0019
63	0.0082	0.0667	$< 10^{-4}$	0.0724	0.0973	0.0046
64	0.0628	0.0678	$< 10^{-4}$	0.1230	0.1371	0.0024
65	0.0473	0.0682	$< 10^{-4}$	0.1073	0.1261	0.0029
66	0.0231	0.0696	$< 10^{-4}$	0.0870	0.1103	0.0037
67	0.0855	0.0881	$< 10^{-4}$	0.1751	0.1706	0.0013
68	0.0082	0.0878	$< 10^{-4}$	0.0942	0.1161	0.0942
69	0.0645	0.0896	$< 10^{-4}$	0.1516	0.1558	0.0017
70	0.0360	0.0899	$< 10^{-4}$	0.1213	0.1359	0.0025
71	0.0249	0.0898	$< 10^{-4}$	0.1106	0.1285	0.0028
72	0.0489	0.0907	$< 10^{-4}$	0.1355	0.1454	0.0021
73	0.0380	0.1121	$< 10^{-4}$	0.1482	0.1537	0.0018
74	0.0083	0.1112	$< 10^{-4}$	0.1183	0.1339	0.0026
75	0.0248	0.1123	$< 10^{-4}$	0.1350	0.1451	0.0021
76	0.0650	0.1141	$< 10^{-4}$	0.1811	0.1744	0.0012
77	0.0498	0.1138	$< 10^{-4}$	0.1631	0.1631	0.0015
78	0.0098	0.1338	$< 10^{-4}$	0.1429	0.1503	0.0019
79	0.0383	0.1354	$< 10^{-4}$	0.1743	0.1701	0.0013
80	0.0247	0.1374	$< 10^{-4}$	0.1617	0.1622	0.0015

Table A.7: Equilibrium configurations for pH $3-4$ (cont.)